Nanotechnology, Science and Applications

Dovepress
Taylor & Francis Group

Open Access Full Text Article

ORIGINAL RESEARCH

A Cost-Effective Approach to Triphenylamine-Assisted Fabrication of Stable Cu_2O Nanoparticles: Structural Analysis and Multifunctional Antibacterial, Optical, and Electronic Performance

Omid Azizian-Shermeh, Ali Reza Modarresi-Alam, Ebrahim Mollashahi, Sahar Shabzendedar

Organic and Polymer Research Laboratory, Department of Chemistry, Faculty of Sciences, University of Sistan and Baluchestan, Zahedan, Iran

Correspondence: Ali Reza Modarresi-Alam, Organic and Polymer Research Laboratory, Department of Chemistry, Faculty of Sciences, University of Sistan and Baluchestan, Zahedan, Iran, Tel +9854333431146; +989153414338, Fax +985433446565, Email modaresi@chem.usb.ac.ir

Introduction: Research interest in nanomaterials has surged because of their unique physical and chemical characteristics that differentiate them from their bulk counterparts, such as electrical resistivity, strength and hardness, chemical reactivity, optical and electronic properties and a wide range of adaptable biological activity. The primary objective of this study was to develop a facile and cost-effective method for the triphenylamine-assisted synthesis of stable copper (I) oxide (Cu_2O) nanoparticles (NPs) and to comprehensively evaluate their potential optical, electronic, and antibacterial applications. This present study is the first report of a facile and effective method to triphenylamine-assisted synthesis of stable copper (I) oxide (Cu_2O) nanoparticles (NPs).

Methods: After triphenylamine-assisted synthesis of Cu_2O NPs, the synthesized NPs were comprehensively characterized through X-ray diffraction (XRD), transmission electron microscopy (TEM), scanning electron microscopy (SEM), UV-Vis spectroscopy, Fourier-transform infra-red spectroscopy (FTIR), atomic force microscopy (AFM), and thermal gravimetric analysis (TGA). The antimicrobial activity of the Cu_2O NPs was evaluated using the disk diffusion method and determination of minimum inhibitory concentration (MIC) against four clinically significant bacterial strains.

Results: XRD analysis confirmed the crystalline cubic structure of Cu_2O NPs, while TEM and SEM revealed spherical morphology with an average particle size of 10–60 nm with the highest frequency of 30 nm in diameter. Optical, electronic and antimicrobial properties of Cu_2O NPs were also studied. UV-Vis spectra exhibited a distinct absorption peak at 275 nm and 280 nm in formic acid and N-methyl pyrrolidone (NMP) solvents, respectively. Electronic properties were investigated using cyclic voltammetry (CV) analyses and electron transitions (direct and indirect) in UV-Vis. Results of antibacterial activities indicated dose-dependent inhibition. The synthesized NPs showed significant efficacy, particularly against Gram-positive bacteria.

Conclusion: These findings highlight the potential of stable Cu_2O NPs as durable antimicrobial agents for biomedical and its electrical and optical characteristics making it appropriate for various uses in photovoltaics, sensors, and photocatalysis and industrial applications, offering enhanced longevity and effectiveness compared to conventional counterparts.

Keywords: antimicrobial properties, copper (I) oxide nanoparticles, electronic properties, optical properties, triphenylamine, tetraphenylbenzidine

Introduction

Nanomaterials, with their unique properties at the nanoscale (1–100 nm), are revolutionizing the field of biotechnology.[1] Research interest in nanomaterial has surged because of their unique physical and chemical characteristics that differentiate them from their bulk counterparts, such as electrical resistivity, strength and hardness, chemical reactivity, optical and electronic properties and a wide range of adaptable biological activity.[2–5] The vast range of uses for metal

https://doi.org/10.2147/NSA.S571946
Received: 4 October 2025
Accepted: 11 February 2026
Published: 11 April 2026

Graphical Abstract

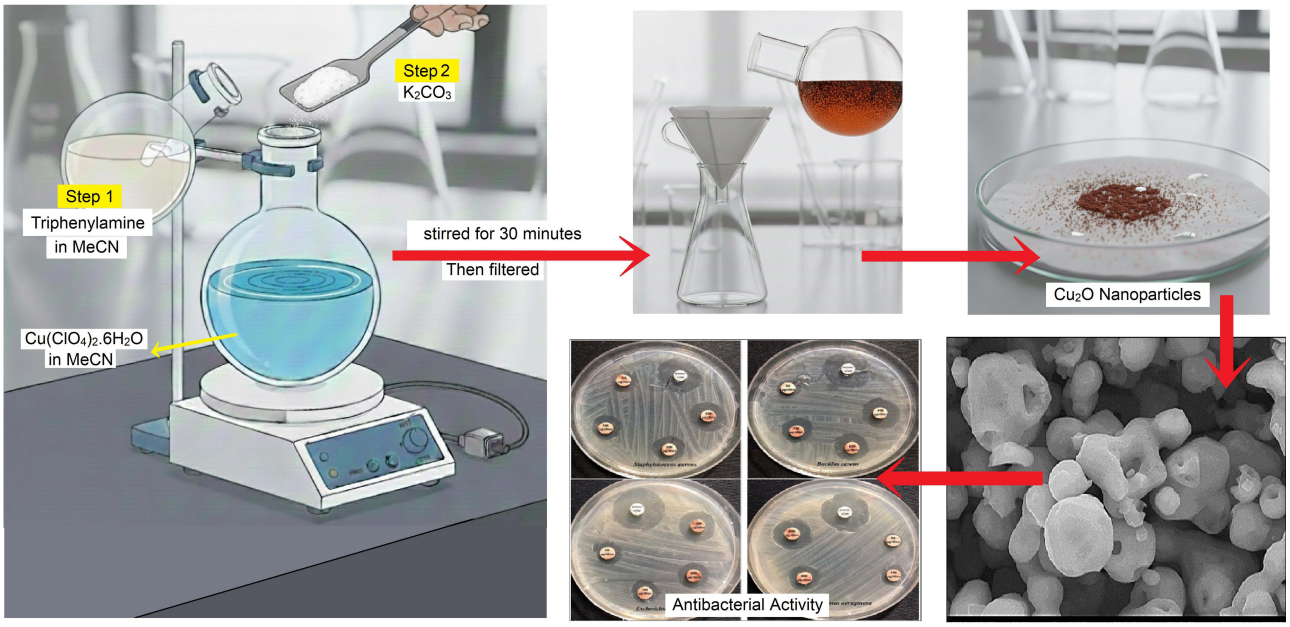

oxide nanoparticles (NPs), including medicinal applications, disinfectants, industrial catalysts, fillers, opacifiers, antimicrobials, medical devices, and the development of microelectronics and cosmetics, has drawn special attention to them.[2–6] Metal oxide NPs, such as copper oxide, have attracted attention and may be used in various biological domains due to their antibacterial and biological properties.[7–9] Copper oxide NPs are available in two types, cubic configuration of cupper (I) oxide (Cu_2O),[10] which has an average band gap of 2.17 eV, and cupric oxide (CuO) monoclinic crystalline[11] which has a narrow band gap of 1.2 eV. Cu_2O crystallizes as a simple cubic with a lattice constant of around 4.27 Å. One cubic sublattice (bcc) of oxygen anions and two cubic sublattices (fcc) of copper cations. Four copper atoms coordinate each oxygen atom tetrahedrally, yet two oxygen atoms coordinate each copper atom linearly.[12] Cu_2O's distinct electrical and optical characteristics stem from this structure, making it appropriate for various uses in photovoltaics, sensors, and photocatalysis.[13] Nano-sized copper oxides, specifically CuO and Cu_2O, are considered potentially valuable materials for converting and storing energy applications due to their unique properties. Because of their nano size, they have a larger surface area and greater reactivity, which makes them ideal for use in photovoltaics, catalysts, and energy storage systems.[14] Cu_2O has potential uses due to its electrical characteristics, including photocatalysis,[15] biosensors,[16] storage devices,[17] electrode materials,[18] solar energy conversion,[19] and antibacterial activities.[20] Several methods, including chemical reduction,[21] hydrothermal synthesis,[22] microemulsion method,[23] electrochemical,[24] sonochemical,[25] microwave irradiation,[26] and photochemical synthesis[27] have been used to synthesize metal and metal oxide nanoparticles, especially Cu_2O. However, each of these methods has some advantages and disadvantages. For instance, the chemicals used in these processes have raised concerns due to their potential environmental damage.[28] In the chemical reduction method, oxidation of final product which leads to compound phases (Cu, Cu_2O, CuO), using toxic and dangerous reagents (eg, sodium borohydride, hydrazine, etc.) which can cause environmental and safety concerns and can be harmful, dangerous and costly to careful disposal is very challenges.[29,30] In the synthesis of sol-thermal (hydrothermal/solvothermal) method, need for high pressure or temperature which requires high energy consumption, the use of dangerous chemical materials, the formation of particles as poly-disperse and aggregated particles due to good crystal growth, long reaction time up to several hours or several days, sensitive to small changes in parameters such as pH, temperature, solvent or pre-material concentration which influence on the size and shapes of nanoparticles and be difficult to make pure processing after

synthesis are the challenges of this method.[31–33] In the synthesis of photochemical process, precise control of light parameters such as wavelength, intensity and time, use of organic solvents and photo-initiators, requires intensive care, need for visible light sources or UV specialized light sources that have high cost for setup and consumption of energy, low variation in defined morphology and poor crystallization in comparison with other methods such as sol-thermal are the main challenges of this method.[32,33] However, the present study and the method that had used in it do not have any of the disadvantages mentioned in the above methods, and this is considered an important advantage for this method and another advantage is that this method is known as a "green" process that do not require any additional reducing or stabilizing agents, as reduction, crystallization, and stabilization occur simultaneously.[34] Numerous scientists have created a wide range of Cu_2O micro and nanostructures, including nanoflowers,[35] nanourchins,[36] nanowires,[37] nanospheres,[38] nanosheets,[39] nanorods,[40] and hollow spheres[41] by several methods that been explain above. Mallik et al (2020) synthesized Cu_2O NPs using chemical precipitation method in an aqueous solution. Sodium borohydride was used as the primary reducing agent, and polyethylene glycol was used as the capping agent. The average size of the synthesized Cu_2O NPs was measured to be about 7.5 ± 1.8 nm.[42] Spiridonov et al (2020) reported a one-step room-temperature synthesis of Cu_2O NPs in a carboxymethyl cellulose (CMC) matrix. They used $NaBH_4$ as a reducing agent and CMC as a stabilizing polymer matrix to reduce copper sulfate. The Cu_2O NPs were approximately 10 nm in diameter.[43] Liu et al (2021) described how they synthesized Cu_2O NPs through a hydrothermal technique. They obtained different morphologies, including cubic, octahedral, and urchin-like, by adjusting the content of polyvinyl pyrrolidone as a template. The synthesized Cu_2O NPs were used for the electrochemical reduction of CO_2 to alcohols.[44] Salgado et al (2024) synthesized Cu_2O NPs using a green synthesis method with the help of *Eucalyptus globulus* leaf extract on cellulose-based fabric. This method involved the reduction of Cu^{2+} to Cu^{+}, and the size of the synthesized Cu_2O NPs ranged from 34.0 to 173.5 nm with an average diameter of 81.84 nm.[45] Ahmadi et al (2024) synthesized Cu_2O NPs using an electrochemical method. The researchers studied the effect of electrolyte composition (NaCl, Na_2SO_4, and CTAB) on the formation of Cu_2O NPs using copper electrodes. The size of the Cu_2O NPs varied depending on the synthesis conditions but was generally less than 100 nm.[24] Studies have shown that certain compounds like amines can enhance the stability of metal oxide NPs by formation of complex and acting as coating agents and attaching to their surface through physical or chemical adsorption. The amine coating creates spatial and electrostatic repulsion between NPs, preventing aggregation and sedimentation, thus improving their colloidal stability.[46] In addition to amines, other compounds, such as organic compounds like polymers, surfactants, and ligands, as well as inorganic compounds like silica and metal oxides, can also contribute to the stability of metal oxide NPs.[47,48] Numerous articles have reported the synthesis of metal and metal oxide NPs in the presence of amines.[34,49–52] For instance, Aslam et al (2007) described a straightforward one-step method using dodecylamine to synthesize iron oxide nanoparticle aqueous colloids.[46]

Furthermore, the development of durable antibacterial agents is crucial for biomedical and industrial applications. Unlike organic antibacterial agents, which often suffer from poor stability and heat resistance, inorganic metal oxide nanoparticles offer superior durability and longevity. From an economic perspective, the fabrication process of antimicrobial agents must be cost-effective to be viable for large-scale applications. The use of copper and copper oxide, an abundant and relatively inexpensive compound compared to another metal and metal oxides such as silver or gold, combined with a facile synthesis route, presents a significant economic advantage for developing potent antibacterial materials. Therefore, the creation of novel nanomaterials using new synthetic techniques has emerged as a key area in recent approaches to nanotechnology. The production of innovative metal oxide-based nanomaterials for biological applications has made new advancements, as described in this account.[49,53] In this work, high-purity Cu_2O nanoparticles were synthesized from Cu $(ClO_4)_2$ in the presence of triphenylamine (TPA) as a reducing and synthesis of its dimer as stabilizing agent. As-prepared Cu_2O NPs were characterized in size, structure, surface, antimicrobial, optical and electronic properties. The Cu_2O NPs exhibited significant effective against every bacterial strain tested, with indicating a dose-dependent response. Other advantage of the method is that dimer of TPA (tetraphenylbenzidines; TPB) as other useful product is generated in the reaction. TPB is an important organic compound and has various applications in xerography, photoconductors and hole-transporting layers in organic solar cells, organic light emitting diodes (OLED), organic field effect transistors (OFETs), etc.[54–56]

Methods and Materials

Chemical Materials and Microorganisms

All of the chemical materials used in this study were purchased with high purity (all solvents were GC and HPLC grade) from Merck (Germany) and Sigma-Aldrich (USA). TPA (high purity), acetonitrile (MeCN) (≥99.8%), sodium hydroxide (NaOH) (high purity), n-hexane (≥98.0%), dichloromethane (≥99.8%), chloroform (≥99.8%) and potassium carbonate (K_2CO_3) (high purity) were bought from Merck and tetrabutylammonium perchlorate (Bu_4NClO_4) (≥98.0%), Copper (II) perchlorate hexahydrate [Cu $(ClO_4)_2.6H_2O$] (≥99.0%) were bought from Sigma-Aldrich. It should be noted that for more caution, MeCN, n-hexane, chloroform and dichloromethane had been distilled before used. The bacteria *Bacillus cereus* (ATCC 11778), *Staphylococcus aureus* (ATCC 6538), *Pseudomonas aeruginosa* (ATCC 27853), and *Escherichia coli* (ATCC 25922) were received from the Iranian Research Organization for Science and Technology (IROST), Tehran, Iran. Double-distilled water was used for washing the laboratory dishes.

Synthesis of Cu_2O NPs

About 6 mmol (2.223 g) of Cu $(ClO_4)_2.6H_2O$ was first dissolved in 100 mL of MeCN. This solution was then added to 4 mmol (0.98 g) of TPA dissolved in 200 mL of MeCN. Immediately upon mixing the two solutions, the color of the mixture turned dark blue. The mixture was stirred at room temperature for 12 hours on a magnetic stirrer. After 12 hours, 5 g of K_2CO_3 and 10 mL of double-distilled water were added to the mixture and stirred for 30 minutes (pH=12–13). During this time, orange particles appeared in the mixture, and the mixture's color altered to dark brown-red. The solid particles were filtered through filter paper and washed with 50 mL chloroform. At the bottom of the flask, a dark brown-red precipitate of Cu_2O NPs remained, which did not dissolve in the hexane-dichloromethane phase (hexane-dichloromethane phase was used for washing and workup the Cu_2O NPs). This precipitate was collected and stored after drying after drying in an oven between 45 and 50°C for a duration of 12 hours. The chemical reaction for preparing of Cu_2O NPs in the presence of TPA is presented in Scheme 1.

Characterization of Cu_2O NPs

Synthesized NPs were determined by analysis of UV–Vis spectra in the range of 200–1100 nm using a UV–Vis spectrophotometer (Agilent, U.S.A, Cary 60 software) was used to record the UV–Vis spectra of 0.02 gL^{-1} solution of synthesized powder in N-methylpyrrolidone (NMP) and formic acid (FA) solvents. The crystal structure of the Cu_2O NPs was analyzed using recording their elemental spectra using an X-ray diffractometer (XRD; D8-Advance Bruker, Germany). This device used a copper K-alpha radiation source with a wavelength of 1.54 Å, scanning over an angle range of 0 to 80 degrees, and operated at 40 kV and 30 mA. The average size of the Cu_2O crystallites was estimated using Scherrer's equation: $D = 0.9\ k/b\ \cos\theta$. Where D is the particle size in nanometers, k is the X-ray wavelength (0.154 nm), b is the full width at half maximum (FWHM) of the diffraction peak, and θ is the diffraction angle.

Fourier transform infrared (FTIR) spectroscopy was also performed on the Cu_2O NPs using a Spectrum RXI instrument (PerkinElmer, USA) scanned over wavelengths between 400 and 4000 cm^{-1} with a 4 cm^{-1} separability. For the FTIR measurements, potassium bromide (KBr) powder was combined with the dried nanoparticle samples and pressed into a pellet for analysis. To investigate the performance and thermal stability of the synthesized Cu_2O NPs, thermal gravimetric analysis was conducted to determine thermal stability, decomposition behavior, and compositional purity of Cu_2O NPs (Sanaf Electronic Industries Company TGA (DMTA-1000)) was used with a temperature program of 23–600 °C and 34–600 °C at a heating rate of 10 °C/min for an atmosphere of air (O_2) and nitrogen (N_2), respectively.

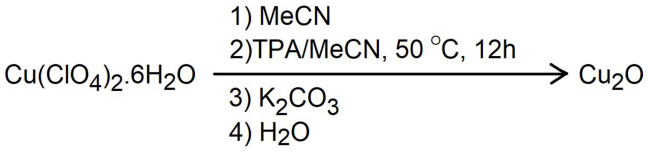

Scheme 1 Synthesis of Cu_2O NPs in the presence of TPA.

Cyclic voltammetry (CV) technique for investigating the electrochemical behavior of Cu_2O NPs was conducted in a three-electrode cell containing 1.0 M NaOH electrolyte. A carbon paste electrode (0.194 g graphite + 0.006 g NPs powder + two drops of paraffin) was prepared as working electrode. The counter electrode was a platinum wire, while the reference electrode was an Ag/AgCl electrode. The CV profile for determination of band gap energy was recorded by the electrodes used were glassy carbon electrode (GCE) as the working electrode, Ag/AgCl as the reference electrode, and Pt wire as the auxiliary electrode. The analysis media was Cu_2O NPs added to CH_3CN solution of Bu_4NClO_4 (0.1 M) electrolyte under N_2 atmosphere. The surface properties of the synthesized nanoparticles were examined using atomic force microscopy (AFM) (AFM-Brisk).

Antibacterial Activity

The antibacterial efficacy of synthesized Cu_2O NPs was studied using both the disk diffusion and the minimum inhibitory concentration (MIC) methods[57] against four clinically significant bacterial strains: *Pseudomonas aeruginosa* (ATCC 27853), *Bacillus cereus* (ATCC 11778), *Escherichia coli* (ATCC 25922), and *Staphylococcus aureus* (ATCC 6538). For the disk diffusion assay, bacterial cultures were grown in Mueller-Hinton Broth (MHB) and standardized to 0.5 McFarland standard (approximately 1.5×10^8 CFU/mL). The bacterial suspension was then inoculated onto Mueller-Hinton Agar (MHA) plates using a sterile swab. Sterile filter paper disks (6 mm diameter) impregnated with Cu2O NPs (50, 100, 200, and 400 µg per disk) were placed on the plates. Amoxicillin-Clavulanic acid (30 µg) disks served as a positive control. The plates were incubated at 37 °C for 24 hours. The diameter of the inhibition zone (ZOI) was measured in millimeters. The MIC was assessed through the broth micro dilution procedure in 96-well plates. Serial dilutions of nanoparticles (ranging from 12.5 to 800 µg/mL) were prepared in MHB, and standardized bacterial suspensions (5×10^5 CFU/mL final concentration) were added. Positive controls (bacteria without NPs) and negative controls (medium only) were included. Bacterial growth was assessed by measuring optical density at 600 nm after 24 hours of incubation at 37 °C. The MIC was defined as the lowest nanoparticle concentration that completely inhibited visible bacterial growth. All experiments were performed in triplicate, and the results for Zone of Inhibition are expressed as mean ± standard deviation (SD).

Results and Discussion

Synthesis and Mechanism

The present study is the first report of a facile and effective method to synthesize stable Cu_2O NPs from Cu^{2+} by TPA as a reductant reagent. The similar method was applied to yield TPB.[58] In fact, we were obtained Cu_2O NPs addition to TPB which we wish to report in this paper. In other word, we are prepared for both products. Characterization of TPB was before reported by Sreenath et al.[59,60] The proposed mechanism for the preparation of Cu_2O NPs in the presence of TPA is presented in Scheme 2. This scheme is based on reports that have provided mechanisms for the electrochemical oxidation of TPA.[58,59] Here, Cu_2O NPs were prepared with TPA, and two steps are considered the mechanism. In the first step, TPA loses an electron and converts to a cationic radical. Simultaneously, Cu^{2+} ions capture the electron lost from TPA and are reduced to Cu^+. In the second step, the two formed cationic radical's couple together and convert to TPB by losing two protons. Then, two Cu^+ ions react with a K_2CO_3 in water to convert to Cu_2O NPs.[56] In the other words, formation of TPB dimer as other product during reaction can stabilize Cu^+ for formation Cu_2O. As presented in the proposed mechanism, the dimer produced forms a complex with Cu^+, preventing its oxidation to Cu^{2+} (and sequentially to CuO), and upon addition of K_2CO_3, Cu_2O nanoparticles are formed. In fact, TPA not only act as reducer reagent but also as stabilizer (as formation of its dimer). As mentioned before, various studies have demonstrated and reported the stabilization of metals and metal oxides, especially copper and copper oxide, by amine groups.[34,49–52]

Characterization

FT-IR Spectroscopy Analysis

FT-IR spectrum was recorded at room temperature to evaluate the structural and chemical nature of Cu_2O NPs. Figure 1a and b showed the FT-IR analysis of the synthesized Cu_2O NPs compared with Cu_2O NPs that prepare from Sigma-Aldrich

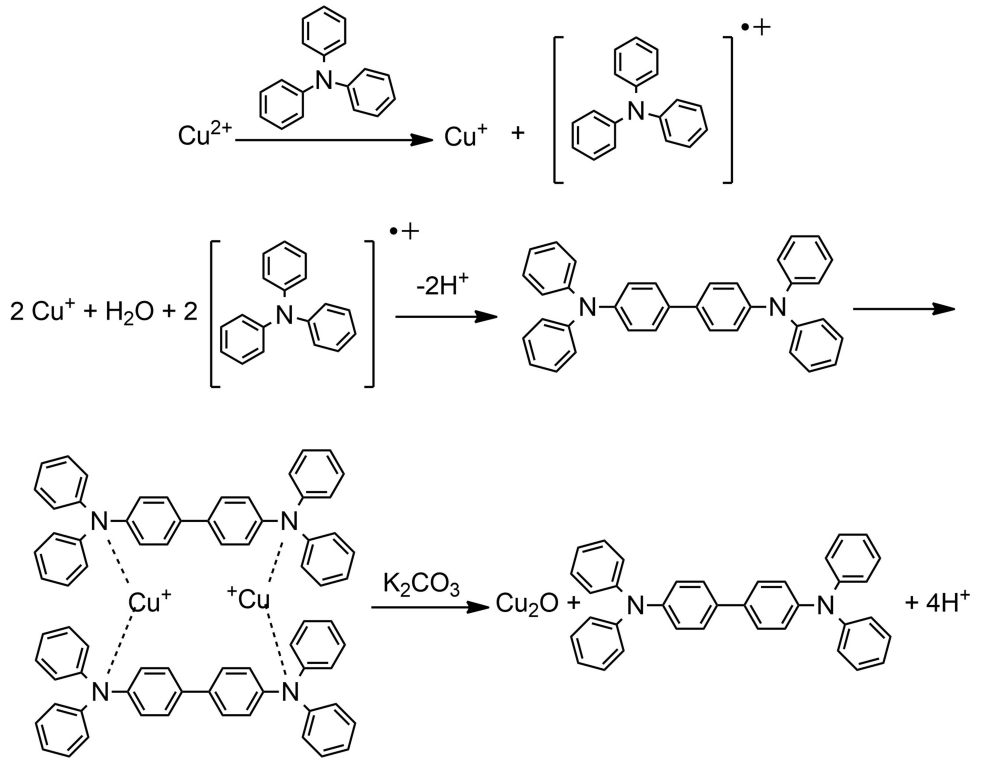

Scheme 2 Mechanism of reaction and stability of Cu^+ during Cu_2O NPs preparation.

Company respectively. To characterize the synthesized Cu_2O NPs by examining the stretching and bending vibrations of the existing bonds and functional groups. As can be seen, in the FT-IR spectrum of Cu_2O NPs, there is a clear and strong absorption band around 604 cm^{-1} for synthesized Cu_2O NPs and around 603 cm^{-1} for purchased Cu_2O NPs, attributed to the Cu (I)-O vibrational mode. This peak is a strong indicator of the presence of Cu_2O.[60–62] Cu_2O has a strong absorption band around 600–630 cm^{-1}, while CuO has bands around 500–600 cm^{-1}.[63–68] As can be seen, the FT-IR spectra of synthesized NPs are completely confirmed by the purchased NPs and there is a reason for successful synthesis and production of pure NPs. In general, the absence of unexpected bands underscores the sample's purity and successful synthesis.

XRD Studies

The XRD pattern of the synthesized Cu_2O NPs was also investigated to identify the phases and find their diffraction planes, and the recorded XRD spectrum is presented in Figure 2. The XRD pattern of Cu_2O NPs provides information about their crystal phases and crystallinity. The XRD pattern of Cu_2O NPs shows peaks at 2θ values of approximately 29.6°, 36.4°, 42.3°, 61.3°, 73.2°, and 77.1°, which are corresponded to the (110), (111), (200), (220), (311), and (222) planes, respectively, as indicated by the JCPDS card, No. 05-0667, which corresponds to the ICDD database reference template.[69] These peaks indicate the cubic cuprite structure of Cu_2O and reveal a face-centered cubic arrangement.[70,71] These peaks indicate the formation of a single-phase cuprite structure without impurities.[72] The absence of peaks in the range of 35.5° and 38.7°, etc. confirms the purity of the phase. Also, the absence of metallic copper peaks (which are at 43.3°, 50.4°, etc.) would be important because during synthesis, especially if a reducing agent is used, there might be a risk of forming metallic Cu instead of the oxide, this confirms the successful synthesis of stable Cu_2O NPs. The Scherer equation, as shown below, was used to calculate the size of the NPs:[73,74]

$$D = \frac{K\lambda}{\beta\cos\theta} \tag{1}$$

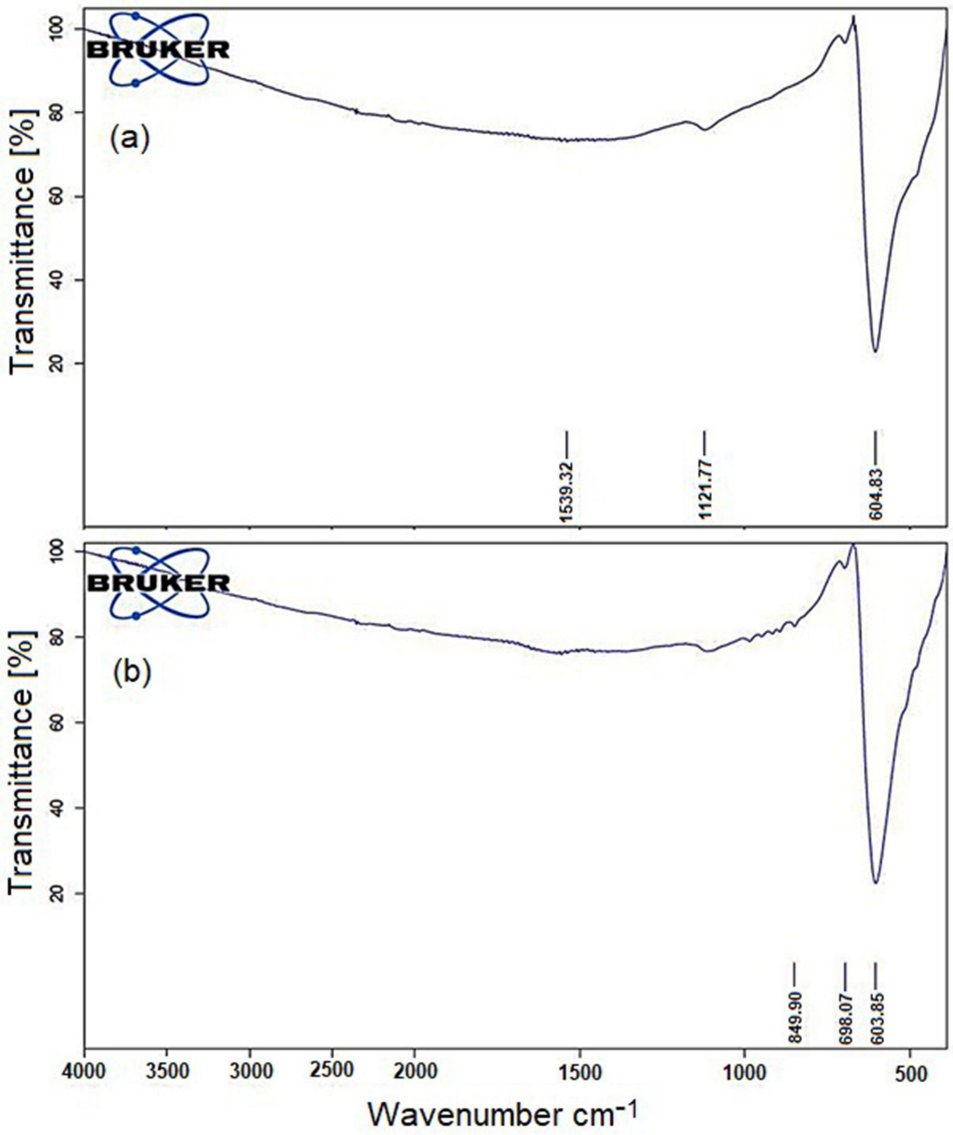

Figure 1 FT-IR spectrum of Cu_2O NPs (**a**) synthesized, (**b**) prepared from Sigma-Aldrich CAS Number: 1317-39-1, Purity ≥ 97%.

Where D is the crystallite size in nanometers, K is the Scherer constant (usually between 0.9 and 1 depending on the NPs shape), λ is the X-ray wavelength (for copper Kα, $\lambda = 1.5406$ Å), β is the full width at half maximum (FWHM) in radians, and θ is the Bragg angle. The angle that shows the highest peak intensity is the Bragg angle (here is 36.4°). According to the equation (1), the size of the Cu_2O NPs is about 33 nm.

EDX Analysis

The EDX and mapping spectra of Cu_2O NPs, which shows the elemental composition of the Cu_2O sample, are shown in Figure 3. In the EDX spectrum, each element has specific energy peaks. For copper, the Kα line is around 8.04 keV, and the Lα line is around 0.93 keV. Oxygen's Kα is around 0.53 keV. So in the spectrum, we should see peaks around these energies. The absence of peaks at other points proves the purity of the synthesized Cu_2O NPs.

The analysis shows that copper constitutes 92.20% by weight and 74.85% by atomic percent, while oxygen comprises 7.80% by weight and 25.15% by atomic percent (Figure 3a). The mapping of Cu_2O NPs that is shown in Figure 3b–d (3b is for Cu, 3c is for O and 3d is for Cu_2O composition) elemental mapping of Cu_2O NPs) completely is compatible with EDX and confirms high purity of Cu_2O NPs.

https://doi.org/10.2147/NSA.S571946

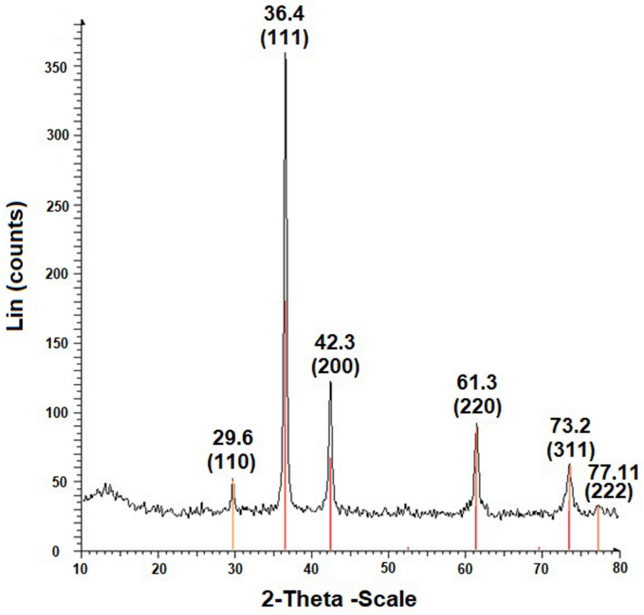

Figure 2 XRD pattern of Cu_2O NPs.

SEM Analysis

SEM image of Cu_2O NPs is shown in Figure 4. SEM is used to get clear, high-definition pictures showing the surface features of a sample. Also SEM would help in looking at their size, shape, and distribution. Figure 4a–d clearly shows the presence of holes in Cu_2O NPs and also different sizes of them. In particular, the histogram of particle size distribution shows that the average diameter of most nanoparticles is approximately 30 nm (fully compatible with XRD) and their size range is from 10 to 80 nm (Figure 4e). The SEM images would show whether the particles are well-dispersed or aggregated. If they are stable, the images should show uniform particles without much clumping. In this study, the synthesized Cu_2O NPs are stable, the image showed uniform particles without much clumping. The spherical or near-spherical nanoparticles are hollow, somewhat similar to the concave spheres reported in the literature,[75] and some areas show the little effects of aggregation.[76]

A notable point in the SEM images is the presence of pores and holes in the synthesized copper oxide nanoparticles. These pores and holes (zeolite-like network) have the ability to absorb small molecules, so they can be used as adsorbents in various processes. Due to the high chemical and thermal stability of the synthesized Cu_2O NPs, these nanoparticles can remain stable at high temperatures and in various chemical environments, which is a very important feature for use in catalysts.[77]

TEM Analysis

The size and shape of the prepared Cu_2O NPs were examined using TEM. The TEM images revealed that the Cu_2O NPs had a uniform spherical shape (Figure 5a). Specifically, a histogram of the particles size distribution showed that the majority of the NPs were approximately 30 nm in diameter, with a size range spanning from 10 to 60 nm (Figure 5b). This size distribution was consistent with the results obtained from X-ray diffraction (XRD) analysis (Figure 3). Furthermore, the TEM images indicated that the generated Cu_2O NPs did not agglomerate, suggesting that they were stable within the observed timeframe.

AFM Analysis

The surface nature of the produced nanoparticles was investigated by AFM to examine the surface roughness of the nanoparticles, and the result is presented in Figure 6. According to Figure 6, the average surface roughness is 10.32 nm, and the surface height is 3.438 μm/div based on the 3D image.[78] The measured roughness of 10.32 nm for a nanoparticle

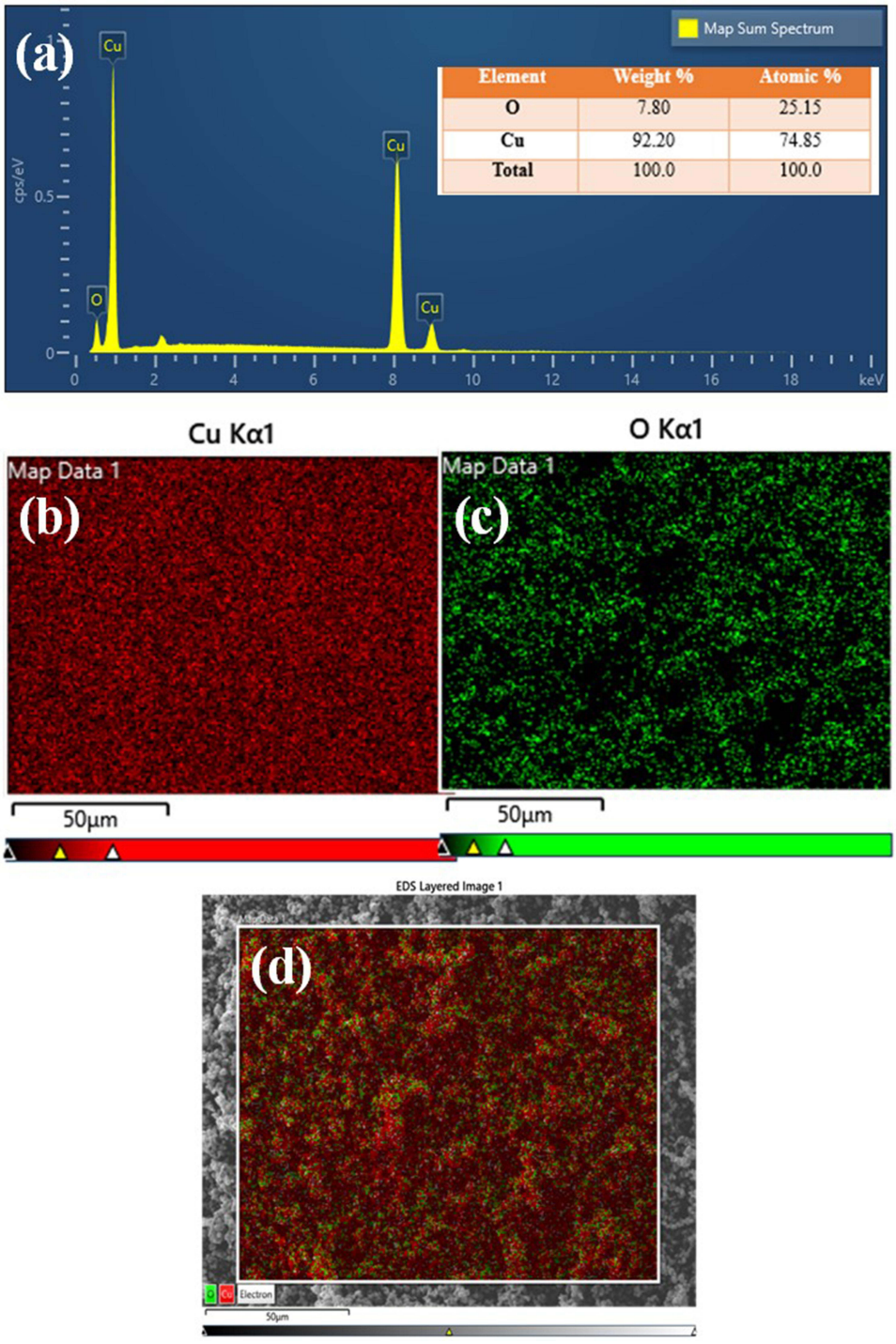

Figure 3 Elemental analysis by (**a**) EDX and (**b–d**) elemental mapping of Cu_2O NPs ((**b**) is for Cu, (**c**) is for O, and (**d**) is for Cu_2O composition.

represents the average deviation of the surface texture from a perfectly smooth plane at the nanoscale. This roughness value, expressed in nanometers, indicates a smooth surface with very low unevenness.[79]

UV-Vis Spectroscopy Analysis and Optical Properties of Cu_2O NPs

The UV-Vis spectral analysis was applied as an important technique for the characterization of the electron transitions property of the Cu_2O NPs. Also, optical properties are crucial for determining a material's suitability in optoelectronic and energy storage devices. To investigate these properties, UV-Vis spectroscopy was employed. Specifically, the technique was used to

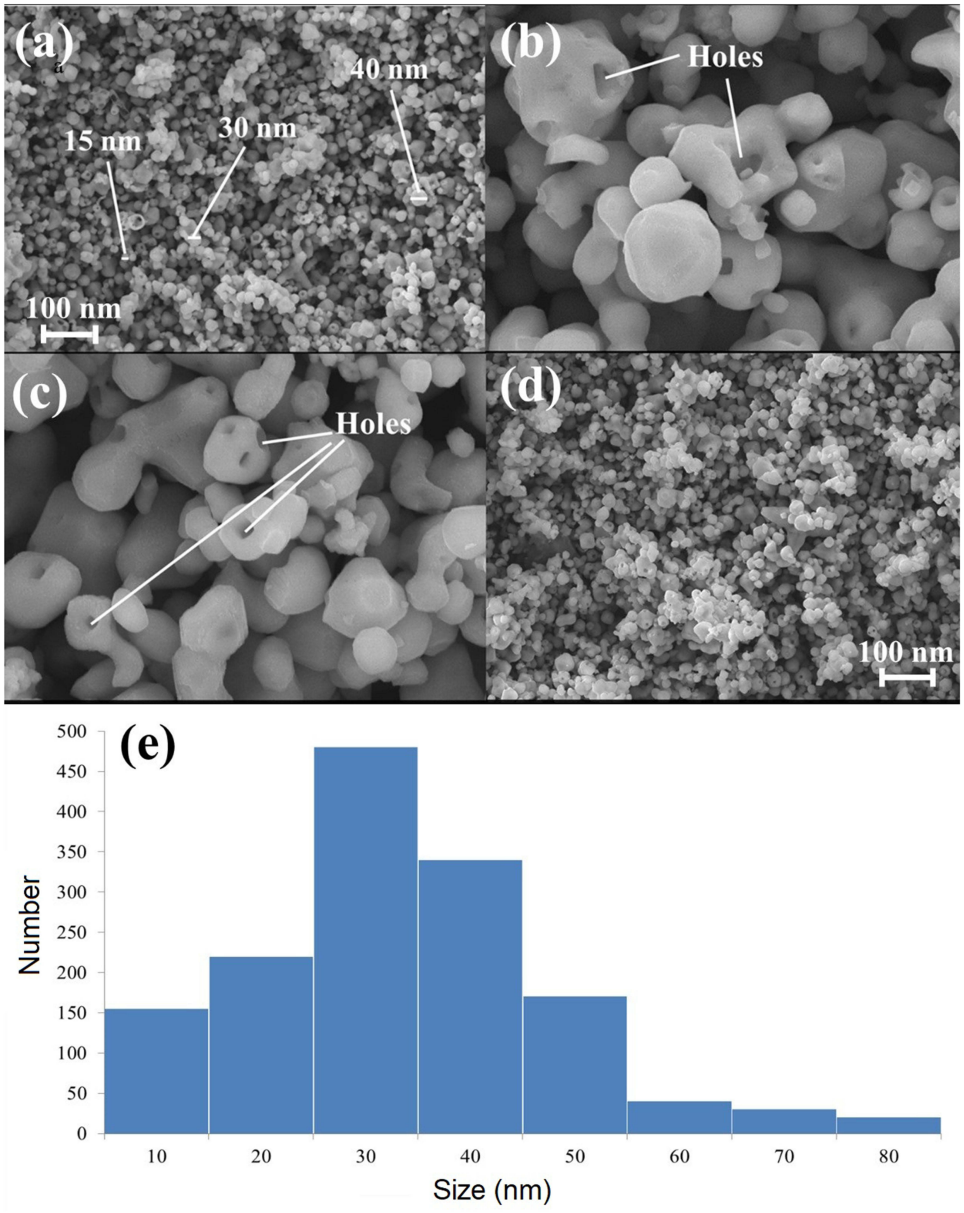

Figure 4 The SEM images (**a–d**) and particle size distribution (**e**) of Cu_2O NPs.

measure the band gap of Cu_2O nanoparticles, with a wavelength range of 200–1100 nm being scanned to record the absorbance spectra. Figure 7a shows the UV-Vis absorption spectra of Cu_2O. Figure 7a depicts absorption peaks at about 275 nm and 280 nm in FA and NMP solvents, respectively, and 785 nm in both them. The peak at 275 and 285 nm is attributed to the characteristic Brillouin transition of Cu_2O.[80] Also the presence of spectral peaks at wavelengths of 275 and nm and 640 nm strongly supports the presence of Cu_2O NPs. Figure 7a shows the absorption spectra of the synthesized Cu_2O NPs, revealing distinct absorption features in both the UV region (275–285 nm) and the visible region (650–750 nm), consistent with previously reported results.[68] This presents bands at 275–285 and 694.8 nm, characteristic of an anisotropic behavior of the Cu_2O NPs. It is important to note that the absorption peak at 275–285 nm arises from interband transitions of copper electrons from a deep level within the valence band.[30] Meanwhile, the peak observed between 650 and 750 nm corresponds to interband transitions of copper electrons from a higher level in the valence band and is identified as the surface plasmon resonance (SPR) peak.[81] The SPR peak of colloidal Cu_2O nanoparticles, previously reported to appear between 600 and 800 nm, matches well with our current findings.[82] Also Dehno Khalaji et al, (2020) reported that, an extremely broad peak at about

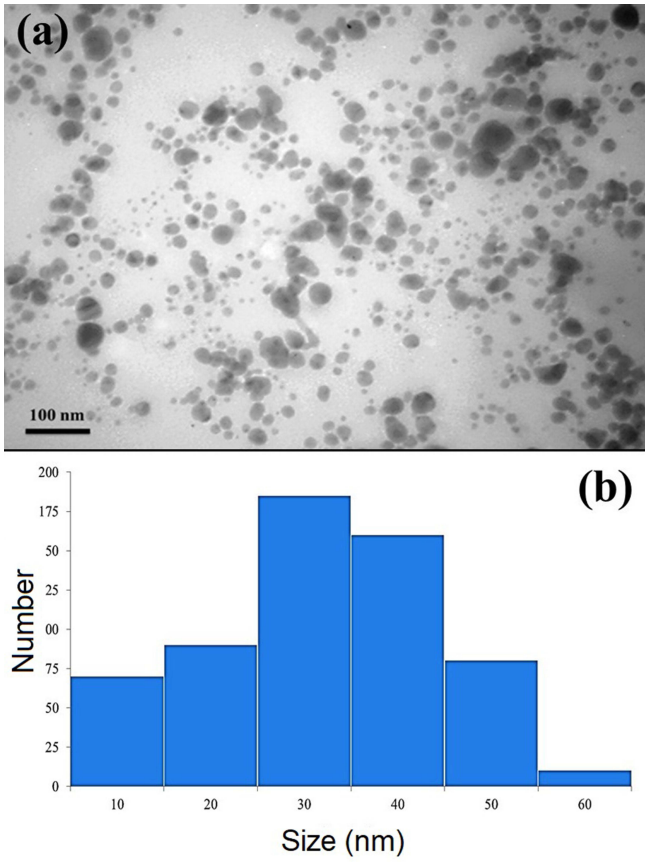

Figure 5 TEM image (**a**) and particle size distribution (**b**) of Cu_2O NPs.

770 nm is corresponded to the d-d transition of the copper ion.[83] The obtained results are comparable with literature.[84,85] The results suggest that Cu_2O NPs were formed after interaction with reducing and stabilizing agent. The optical band gap of Cu_2O nanoparticles can be determined using Tauc's plot, which is based on the equation $(ah\upsilon)^2 = A(h\upsilon - E_g)^n$, where a is the absorption coefficient, υ and $h\upsilon$ is frequency and energy of photon respectively, A is a constant, and n is an exponent that equals 0.5 for direct transitions and 2 for indirect transitions. The E_g is found from the intercept of the $(ah\upsilon)^2$ versus $h\upsilon$ plot on the energy axis. Kumar et al (2021) reported band gap energies (Eg) of 2.18 eV for CuO and 1.62 eV for Cu_2O using this method.[86] In general, the band gap of nanoparticles increases as particle size decreases due to quantum confinement effects.[87,88] However, this trend is not always consistent, as other factors such as structural defects in the oxide form can also influence the band gap. Consequently, the as-synthesized Cu_2O nanoparticles may exhibit a lower band gap.[89,90] The blue shift in optical absorption that occurs with smaller crystallite sizes suggests the influence of quantum confinement, especially when the size is much less than the Bohr radius. The calculated Eg that we got in this work for Cu_2O NPs are 2.70 (indirect transfer mode) and 3.60 eV (direct transfer mode) in NMP and 2.63 (indirect transfer mode) and 3.80 eV (direct transfer mode) in FA solvents as shown in Figure 7b and c, respectively, which is larger than that of bulk Cu_2O (Eg = 2.1–2.2 eV). The difference in properties between a bulk semiconductor and a nanostructured semiconductor is primarily due to quantum confinement effects, which arise when the dimensions of a semiconductor material are reduced to the nanoscale. These effects lead to a quantization of energy levels, altering the material's electronic and optical characteristics.[67,76] This band gap energy is ideally suited for solar cell and optical device and sensors applications.[67,91] This behavior is consistent with the quantum confinement effect. A change from a direct band gap to an indirect band gap can reflect the crystallinity characteristics of the material. Based on the $(\alpha h\upsilon)^n$ versus $h\upsilon$ plots, the results for indirect band gap transitions were found to be more accurate than those for direct transitions. Table 1 shows the E_g for copper oxides NPs in other reports. Also, Figure 7a shows optical band gaps (E_g^{Opt}) of Cu_2O NPs. The E_g^{Opt}(s) were calculated by absorption edges using Equation (2):

https://doi.org/10.2147/NSA.S571946

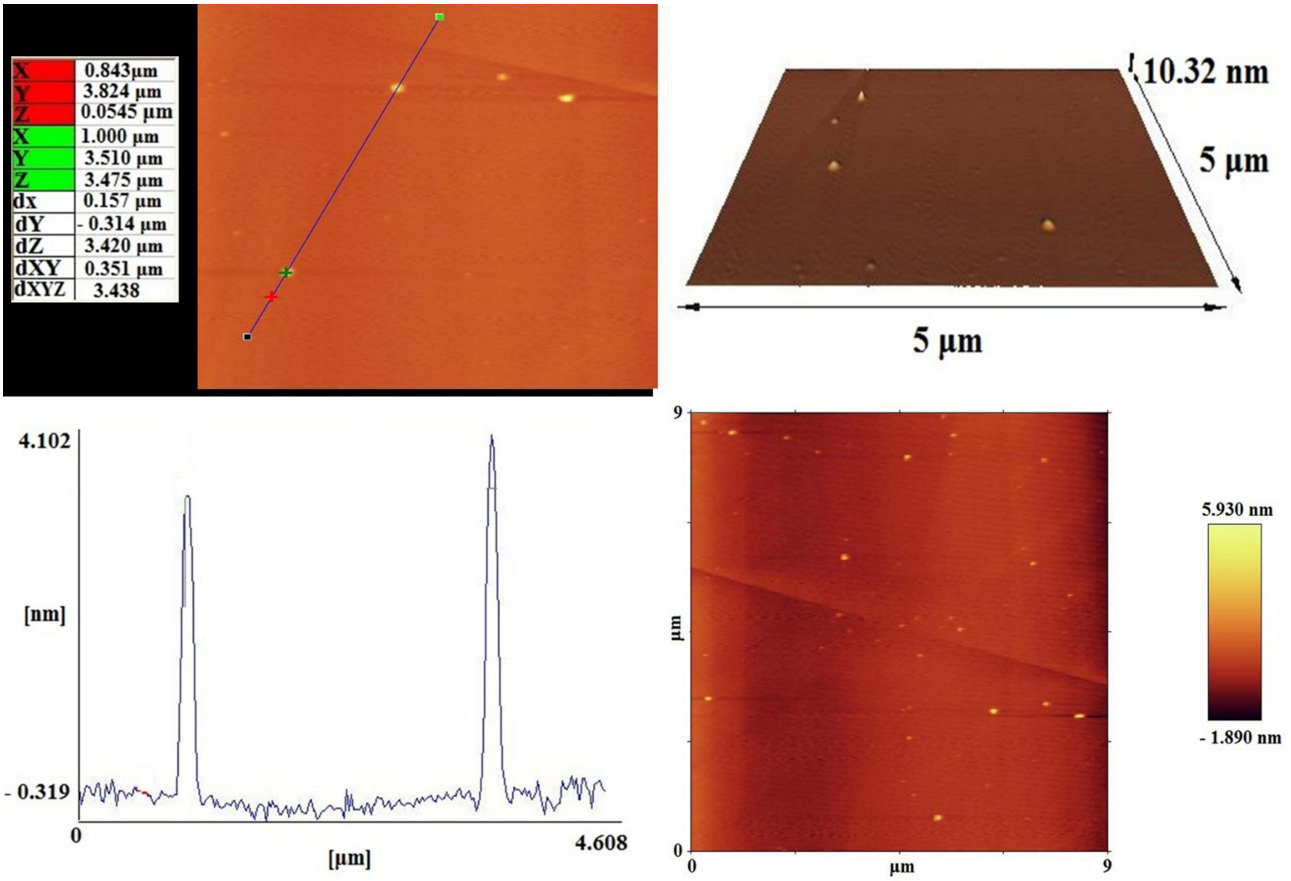

Figure 6 AFM analysis of the Cu_2O NPs surface.

$$E_g^{Opt} = \frac{1242}{\lambda_{onset}} \tag{2}$$

where λ_{onset} is the longest absorption wavelength.[95] The absorption edge for Cu_2O NPs was determined and shown in Table 2. The optical band gap of the Cu_2O NPs in NMP solvent is lower than Cu_2O NPs in FA solvent.[98]

Cyclic Voltammetry

Cyclic voltammetry (CV) is an important electrochemical technique to characterize Cu_2O NPs. CV studies can reveal information about the redox behavior, electrochemical surface area, and catalytic activity of Cu_2O nanoparticles. Specifically, CV can help in understanding the oxidation and reduction processes of Cu_2O. Figure 8 shows the CV curves of Cu_2O NPs recorded using a glassy carbon electrode (GCE) in 1.0 M NaOH solution, within a potential range of –1.0 to 1.0 V (vs Ag/AgCl) at a scan rate of 0.1 $V{\cdot}s^{-1}$. In a basic environment, the Cu_2O redox reaction in a cyclic voltammetry (CV) curve will display both anodic and cathodic peaks. These peaks correspond to the oxidation and reduction of Cu_2O, respectively. The presence of these peaks clearly indicates a reversible redox process that confirms faradaic capacitive properties.[99] These anodic and cathodic peaks are corresponding to the Cu_2O redox reactions as follows:

$$Cu_2O + 2OH^- \Leftrightarrow 2CuO + H_2O + 2e^- \tag{3}$$

$$Cu(OH)_2 + 2e^- \Leftrightarrow CuOH \Leftrightarrow Cu_2O + 2OH^- + H_2O \tag{4}$$

The CV curve indicates that the anodic peak (oxidation) is due to the conversion of Cu_2O to CuO and $Cu(OH)_2$. Conversely, the cathodic peak (reduction) is attributed to the reverse process where CuO and $Cu(OH)_2$ are reduced back

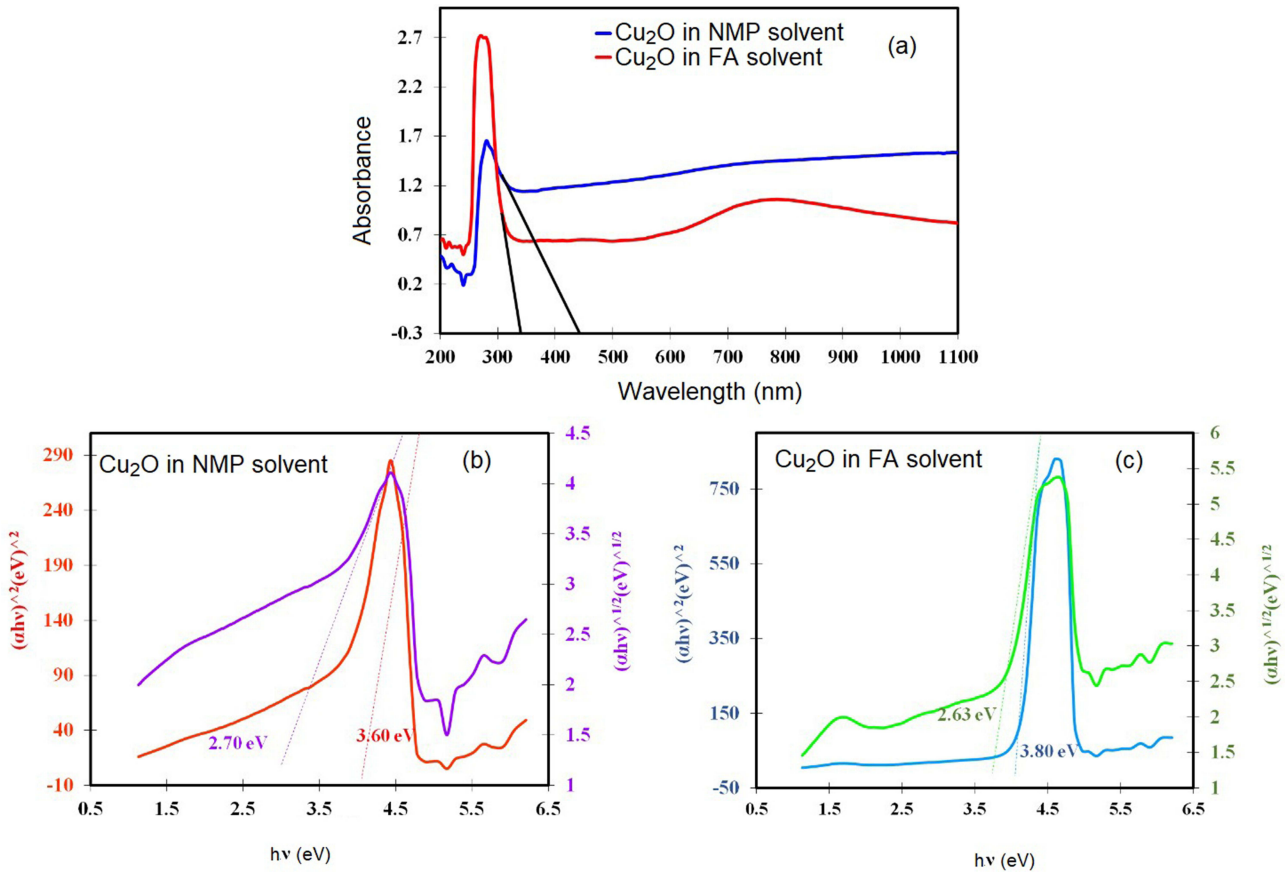

Figure 7 UV-Vis spectra of Cu_2O NPs in formic acid (0.02 $g.l^{-1}$) and NMP (0.02 $g.l^{-1}$) (**a**), plot $(\alpha h\upsilon)^{1/2}$ and $(\alpha h\upsilon)^2$ as a function of $h\upsilon$ of Cu_2O NPs in NMP (**b**), and formic acid solvents (**c**).

to Cu_2O. In simpler terms, the CV curve shows that the material oxidation state changes from Cu_2O to CuO and $Cu(OH)_2$ when voltage is increased, and back to Cu_2O when the voltage is decreased.[100,101] Table 3 shows the current density and potential of the oxidation and reduction peaks of Cu_2O NPs.

Table 1 E_g for Copper Oxides NPs in Other Reports

R	Copper Oxides	Optical E_g (eV) (by $(\alpha h\upsilon)^2$ as a Function of $h\upsilon$)	Ref.
1	CuO NPs	4.2	[62]
2	CuO NPs	4.08	[66]
	Cu_2O NPs	2.07	
3	CuO NPs	3.22	[80]
4	Cu_2O NPs	2.39	[81]
5	Cu_2O NPs	3.67	[82]
6	Cu_2O NPs	2.80	[85]
7	Cu_2O NPs	2.98	[91]
8	Cu_2O NPs	2.00	[92]
9	Cu_2O NPs	2.14	[93]
	CuO NPs	1.35	
10	Cu_2O NPs	1.62	[94]
	CuO NPs	2.18	

(*Continued*)

https://doi.org/10.2147/NSA.S571946

Table 1 (Continued).

R	Copper Oxides	Optical E_g (eV) (by $(\alpha h\upsilon)^2$ as a Function of $h\upsilon$)	Ref.
11	Cu_2O NPs	2.34	[95]
	CuO NPs	1.55	
12	Cu_2O NPs	2.37	[95]
13	Cu_2O NPs	2.08	[96]
	CuO NPs	1.82	
14	CuO NPs	3.25	[97]

Table 2 Absorption Edge and Band Gap Energies of Cu_2O NPs in Different Solvents

Sample in Solvents	Assignments	Absorbance Edge [nm]	E_g^{Opt} [eV]	E_g [by the Plot of $(\alpha h\upsilon)^n$ vs $h\upsilon$] [eV]	
				Direct Band Gap	Indirect Band Gap
Cu_2O NPs in NMP solvent	d → d	450	2.76	3.60	2.70
Cu_2O NPs in FA solvent	d → d	330	3.76	3.80	2.63

Band Gap (Eg), LUMO (Lowest Unoccupied Molecular Orbital) Energies, and HOMO (Highest Occupied Molecular Orbital)

The LUMO and HOMO energies of Cu_2O NPs are fundamental parameters that dictate their electronic and optical behavior, influencing their suitability for various applications. Cu_2O NPs, commonly used in various applications, possess a HOMO-LUMO energy gap that is closely related to their band gap. This gap enabling absorption of a significant portion of the visible light spectrum. The band gap of Cu_2O, which is the energy difference between the valence band (related to HOMO) and conduction band (related to LUMO), is crucial for its optical and electronic properties Cu_2O is a p-type semiconductor, meaning it primarily conducts with "holes" (the absence of electrons). This characteristic is linked to the position of its HOMO and LUMO energy levels relative to the Fermi level.[97] The CV profile for determination of band gap energy was recorded by GCE, Ag/AgCl and Pt wire as working, reference and auxiliary electrodes, respectively. The analysis was conducted using Cu_2O NPs dispersed in a 0.1 M Bu_4NClO_4 electrolyte solution in CH_3CN under N_2 atmosphere. The measurements were taken at a slow potential sweep rate of 0.1 V s^{-1} and a temperature of approximately 25°C. Energy levels were referenced to the standard hydrogen electrode (SHE) by adding 4.4 eV, with the vacuum level considered as zero.[102,103] The experimental results are shown in Figure 9. The electrochemical band gap energy ($E_{g(CV)}$) of the Cu_2O NPs was achieved from analysis of their CV curves. Firstly,

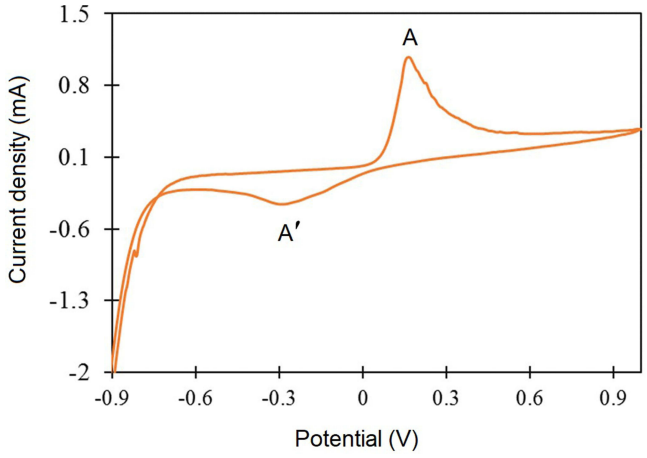

Figure 8 CV obtained at Cu_2O NPs in a solution of 1.0 M NaOH at a scan rate of 0.1 Vs^{-1}.

Table 3 Current Density and Potential of Anodic and Cathodic Peaks for Cu_2O NPs

Compound	Oxidation (A)		Reduction (A′)	
	Epa1 (V)	Ipa1 (μA)	Epc2 (V)	Ipc2 (μA)
Cu_2O NPs	0.179	1.028	−0.28	−0.359

the energy levels of LUMO and HOMO were respectively computed using the reduction and oxidation potential values (equations 5 and 7). After that, Eg^{CV} was determined by subtracting the HOMO energy level from the LUMO energy level, as shown in equation (7):[98,103]

$$E_{HOMO} = -\left(E_{onset}^{Ox} + 4.44\right)eV \tag{5}$$

$$E_{LUMO} = -\left(E_{onset}^{Red} + 4.44\right)eV \tag{6}$$

$$E_g^{CV} = -(E_{HOMO} - E_{LUMO})eV \tag{7}$$

Based on the direct and indirect transfer diagrams and comparing them with the CV results, it can be concluded that since the CV results are consistent with indirect transfer in UV-Vis, the transfer mode is indirect. According to the LUMO $\left(E_{Onset}^{Ox} = +2.00V\right)$ and HOMO $\left(E_{Onset}^{Red} = -1.01\ V\right)$ energy levels, E_g^{CV} was obtained 3.01 eV. This amount is almost similar to E_g that we got in this work for Cu_2O NPs. Using CV, E_{Ox} and E_{Red} of the NPs were found, and the calculated data are summarized in Table 4. The HOMO-LUMO properties of Cu_2O NPs are relevant to their applications in solar cells (as a hole-transport layer), photo catalysis, and other optoelectronic devices.

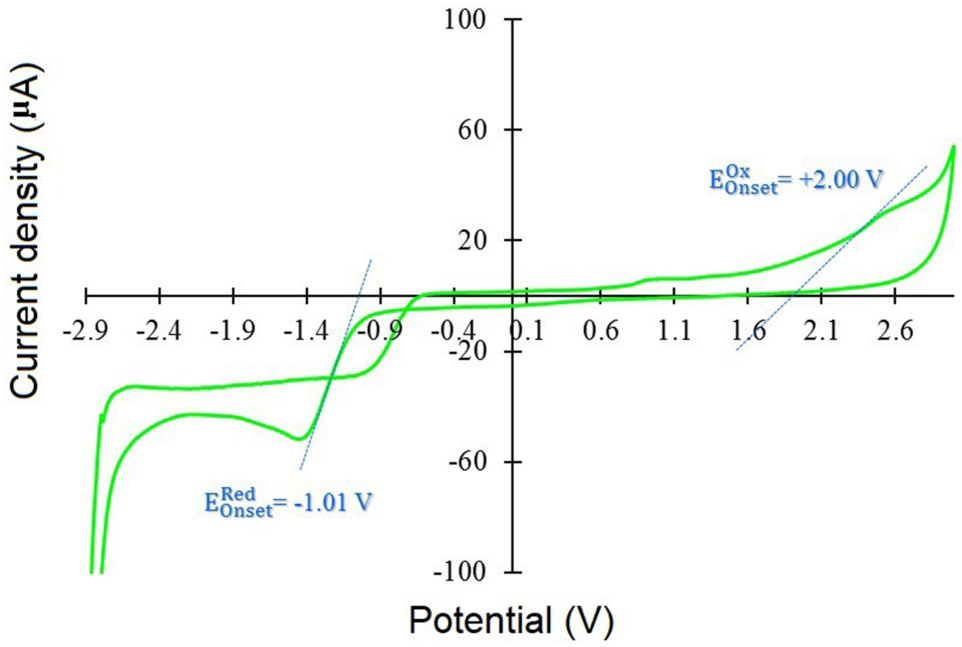

Figure 9 CV of Cu_2O NPs in Bu_4NClO_4 (0.1 M) of CH_3CN solution at a scan rate of (0.1 $V\,s^{-1}$) under an N_2 atmosphere.

https://doi.org/10.2147/NSA.S571946

Table 4 The Frontline Molecular Orbital and Energy Gap of Cu_2O NPs

Sample in Solvents	UV-Vis		CV				
	λ_{onset}	E_g^{Opt} [eV]	E_{onset}^{ox} [V]	E_{onest}^{Red} [V]	E_{HOMO} [eV]	E_{LUMO} [eV]	E_g^{CV} [eV]
Cu_2O NPs in NMP solvent	450	2.76	+2.00	−1.01	−6.44	−3.43	3.01
Cu_2O NPs in FA solvent	330	3.76					

Thermal (TGA) Properties

TGA (and DTG) were used to determine their thermal stability, decomposition temperatures, and any phase changes. TGA is used to evaluate the thermal stability, decomposition behavior, and compositional purity of Cu_2O NPs. This analysis reveals insights into moisture content, organic residue decomposition, and phase transitions (eg, oxidation to CuO or decomposition to metallic Cu) under controlled atmospheres. Maybe also to check for the presence of impurities like organic surfactants or solvents if they were synthesized using a method that leaves residues. In TGA, the heating rate and atmosphere are important parameters. Common atmospheres are nitrogen, argon, or air. If done in an inert atmosphere like N_2, we can observe decomposition without oxidation. In air atmospheres, we can see oxidation effects, like conversion to CuO. Initially, there might be a weight loss due to moisture evaporation. Then, if there are organic surfactants, they would decompose at higher temps, leading to another weight loss step. The main Cu_2O might oxidize to CuO in air. In N_2 atmospheres, maybe decomposition, but Cu_2O is more stable. The decomposition temperature would indicate thermal stability. The DTG and TGA curves of the Cu_2O NPs in N_2 and air atmosphere are presented in Figure 10. According to Figure 10, the DTG and TGA curves show the small lose weight at 70°C which is due to the moisture absorbed (water absorbed physically) by the Cu_2O NPs. According to the DTG curve in air atmosphere, three main stages of weight loss are shown, which are respectively: 70 °C, 170 °C and 250–300 °C. The first weight loss is probably related to the removal of physical water and the second weight loss is related to chemical water that exists as surface hydroxyls or is related to the remaining solvents in the reaction that were used to synthesize Cu_2O NPs.[104] So the TGA curve might show initial and secondary moisture (water absorbed physically and chemically) loss (up to 150$^{°C}$), then maybe oxidation or decomposition of Cu_2O NPs itself at higher temps. If the TGA shows a weight gain, it confirms oxidation to CuO. Alternatively, in N_2 atmosphere, if the sample is pure Cu_2O without organics, the TGA curve might show stability up to a certain temperature, then decomposition to Cu metal and release of O_2, leading to weight loss. NPs might oxidize at lower temps than bulk due to higher surface area. Cu_2O oxidizes above ~250°C. At >600$^{°C}$, Cu_2O may decompose to metallic Cu and O_2 gas.[104]

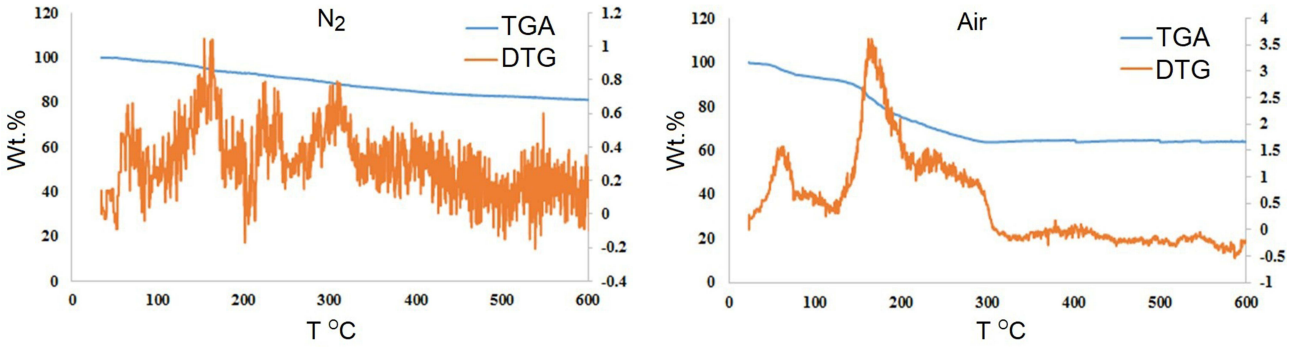

Figure 10 TGA and DTG curves for Cu_2O NPs in N_2 and air atmosphere.

 https://doi.org/10.2147/NSA.S571946

Antibacterial Activity

Cu_2O NPs exhibited significant antibacterial effects against all tested bacterial strains, showing a dose-dependent response. Among the tested bacteria, *S. aureus* showed the highest sensitivity, with the largest inhibition zones observed at all concentrations, while *P. aeruginosa* exhibited the lowest sensitivity. The inhibition zones at the lowest concentration (50 µg/disc) ranged from 7.8 ± 0.1 mm (*P. aeruginosa*) to 11.6 ± 0.2 mm (*S. aureus*) (Table 5 and Figure 11). The results of the MIC assay are also summarized in Table 5. Based on the MIC values, *S. aureus* was the most susceptible strain (MIC = 50 µg/mL), while Gram-negative strains required higher concentrations for inhibition.

Metal oxide nanoparticles (MO NPs) can all stop different types of Gram-positive and Gram-negative bacteria from reproducing, whether they are susceptible or not. As a result, these materials are being considered as possible candidates to combat antimicrobial resistance through modulated action.[105] The synthesized Cu_2O NPs demonstrated potent antibacterial activity against both Gram-positive and Gram-negative bacteria. As shown in Table 5, the Gram-positive strains (*S. aureus* and *B. cereus*) were more susceptible to the nanoparticles compared to the Gram-negative strains (*E. coli* and *P. aeruginosa*). This difference is likely due to the structural variations in the cell wall; Gram-negative bacteria possess an outer lipopolysaccharide membrane that acts as a barrier, limiting the penetration of nanoparticles and ions.[106] Our results are comparable to the standard antibiotic Amoxicillin-Clavulanic acid, although the pure drug showed slightly larger inhibition zones. However, considering the increasing resistance to conventional antibiotics, Cu_2O NPs present a promising alternative. Compared to other studies, our MIC values (50 µg/mL for *S. aureus*) are competitive with those reported for other copper-based nanomaterials. Although direct mechanistic assays were not performed in this study, the antibacterial action of Cu_2O NPs is widely attributed in the literature to three main mechanisms: (1) The release of Cu^+ ions which can bind to DNA and sulfhydryl groups of enzymes, disrupting cellular function; (2) The generation of reactive oxygen species (ROS) such as hydroxyl radicals and superoxide anions upon contact with the bacterial cell, inducing oxidative stress and membrane damage; and (3) Direct physical interaction causing loss of membrane integrity.[107,108] The zeolite-like pores observed in our SEM analysis may further enhance this interaction by increasing the surface area available for ion release. Based on the MIC values of the Cu_2O NPs, *S. aureus* with the lowest MIC (50 µg/mL) showed the highest susceptibility to the nanoparticles, followed by *B. cereus* (100 µg/mL), *E. coli* (200 µg/mL), and *P. aeruginosa* (400 µg/mL). The results highlight the antimicrobial potential of the synthesized NPs, with greater efficacy against Gram-positive bacteria compared to Gram-negative bacteria. The synthesized Cu_2O NPs show strong antimicrobial activity against Gram-positive and Gram-negative bacteria, though the Gram-negative bacteria's outer membrane reduces nanoparticle permeability and limits their effectiveness.[103] Our findings and other studies on Copper and Copper oxide NPs, highlight antimicrobial activity of many metal and metal oxide NPs and their potential as alternatives to antibiotics (Table 6). The antimicrobial activity of Cu_2O NPs is probably caused by the production of ROS, damage to bacterial membranes, and the release of copper ions (Cu^+).[109,110] Compared to other studied NPs, such as ZnO, Ag_2O and Cu_2O NPs offer similar or superior antimicrobial performance and also other benefits such as cost-effectiveness and environmental sustainability. In this study, the stabilized Cu_2O NPs exhibit potent antimicrobial activity against both Gram-positive and Gram-negative bacteria, with greater efficacy against Gram-

Table 5 Antibacterial Activity of Cu_2O NPs: Zone of Inhibition (ZOI) and Minimum Inhibitory Concentration (MIC)

Bacterial Strain	MIC (µg/mL)	Inhibition Zone Diameter (mm) at Different Concentrations (µg/disc)				Positive Control* (mm)
		50	100	200	400	
Staphylococcus aureus	50	11.6 ± 0.2	14.5 ± 0.6	16.9 ± 0.4	19.3 ± 0.4	24.1 ± 0.2
Bacillus cereus	100	10.8 ± 0.4	11.8 ± 0.2	15.2 ± 0.6	18.3 ± 0.7	23.6 ± 0.4
Escherichia coli	200	9.1 ± 0.3	10.6 ± 0.4	12.1 ± 0.2	15.5 ± 0.2	21.5 ± 0.5
Pseudomonas aeruginosa	400	7.8 ± 0.1	9.3 ± 0.1	11.5 ± 0.5	13.2 ± 0.1	20.3 ± 0.1

Notes: Data are presented as Mean ± SD (n=3). *Positive Control: Amoxicillin-Clavulanic acid (Co-amoxiclav) (30 µg/disk).

https://doi.org/10.2147/NSA.S571946

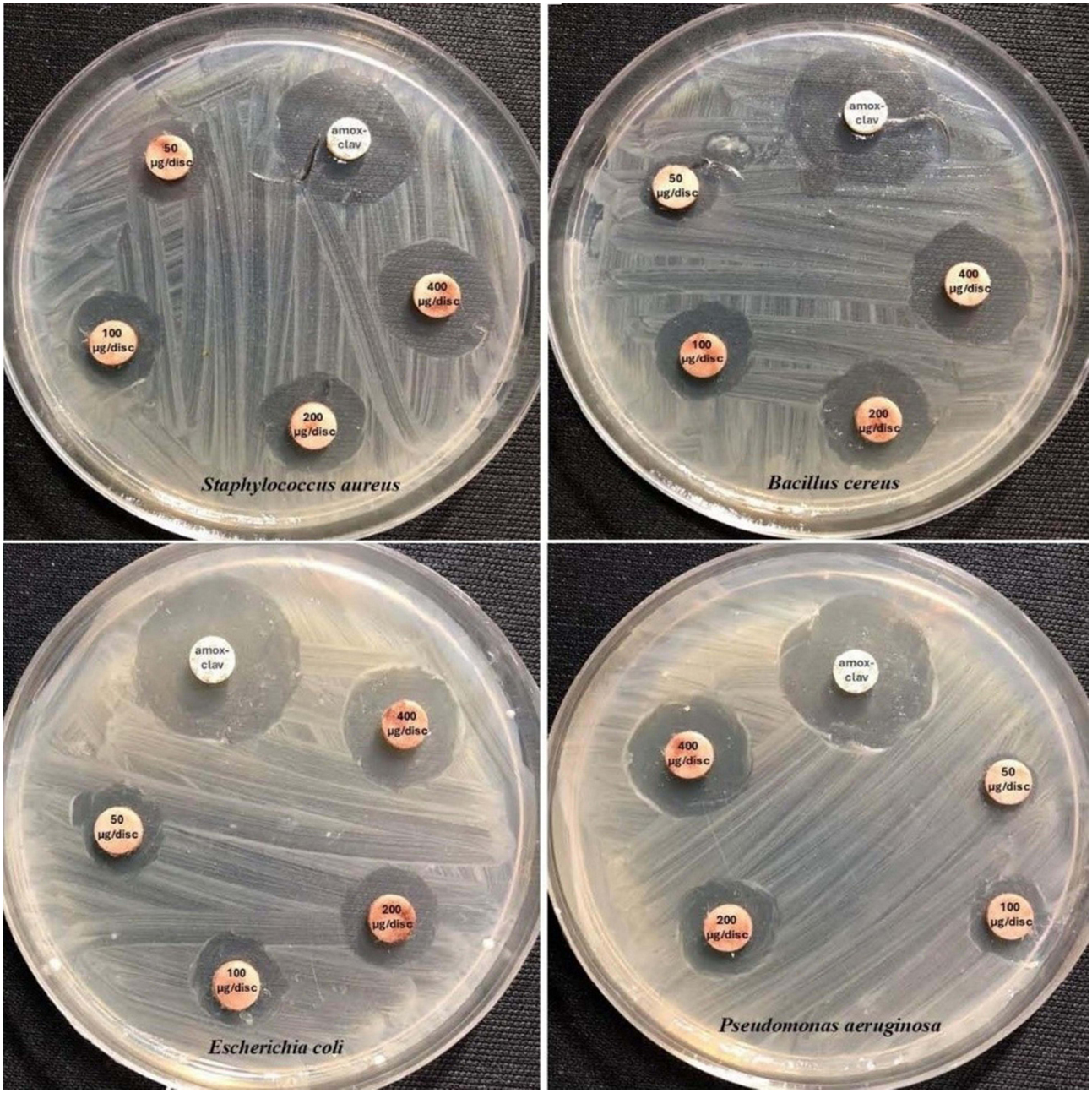

Figure 11 Dose-dependent antimicrobial activity of Cu_2O NPs against pathogenic bacteria.

positive strains. The dose-dependent activity, cost-effectiveness and broad-spectrum potential of these NPs, make them as promising candidates for addressing antimicrobial resistance. However, further studies are needed to assess their safety and applications in healthcare and environmental settings.

Table 6 Commonly Used Copper and Copper Oxide NPs as Antimicrobial Agent, Their Mechanisms of Action and Characteristics

NPs	Proposed Mechanism of Antimicrobial Action	Shape	Size (nm)	The Main Factors That Influence Antimicrobial Activity of NPs	Ref
CuO Cu_2O Cu	Crossing or binding of NPs from the bacteria cell membrane and then damaging the vital enzymes of bacteria	Spherical Irregular Spherical	10–80 70.1–99.3 5–35	Size and Concentration	[111] [112] [113]

Conclusion

In this study, Cu_2O NPs were successfully synthesized using a TPA for the first time, demonstrating a cost-effective and scalable approach for producing nanoparticles with uniform size and morphology. Comprehensive characterization via XRD, SEM, TEM, FT-IR, and AFM confirmed the formation of highly crystalline Cu_2O NPs with size range of 10–80 nm with the highest frequency of 30 nm in diameter. To determine their thermal stability, decomposition temperatures, and any phase changes, TGA and DTG were used. The optical properties, investigated through UV-Vis spectroscopy and electronic properties, were investigated using cyclic voltammetry (CV) analyses and direct and indirect electron transitions in UV-Vis, revealed a band gap energy highlighting their potential for optoelectronic applications and making them promising candidates for integration into energy storage devices, sensors, LED, and solar cell technologies. The antimicrobial efficacy of Cu_2O NPs was evaluated against Gram-positive and Gram-negative bacterial strains, exhibiting significant inhibition of microbial growth at low concentrations. This activity is attributed to the release of copper ions and the generation of ROS, which disrupt cellular membranes and metabolic processes. Collectively, this work underscores the multi-functionality of Cu_2O NPs, bridging their structural, optical, antimicrobial, and electronic attributes. The Cu_2O nanoparticles showed strong antimicrobial effects against all tested bacterial strains, with activity increasing in a dose-dependent manner. Other advantage of the method is that other useful product is generated in the reaction, TPB. It is an important organic compound and has various applications in xerography, photoconductors and hole-transporting layers in organic solar cells, organic light emitting diodes (OLED), organic field effect transistors (OFETs), etc.

Acknowledgment

The authors acknowledge financial support from the Graduate Council and Deputy of Research of University of Sistan and Baluchestan.

Disclosure

The authors report no conflicts of interest in this work.

References

1. Khalil KD, Bashal AH, T Habeeb, et al. Multifunctional lanthanum oxide-doped carboxymethyl cellulose nanocomposites: a promising approach for antimicrobial and targeted anticancer applications. *Int J Biol Macromol*. 2024;283(1):137495. doi:10.1016/j.ijbiomac.2024.137495
2. Sahooli M, Sabbaghi S, Saboori R. Synthesis and characterization of mono sized CuO nanoparticles. *Mater Lett*. 2012;81:169–172. doi:10.1016/j.matlet.2012.04.148
3. Khashan KS, Sulaiman GM, Abdulameer FA. Synthesis and Antibacterial Activity of CuO Nanoparticles Suspension Induced by Laser Ablation in Liquid. *J Sci Eng*. 2016;41:301–310. doi:10.1007/s13369-015-1733-7
4. Thipe VC, Jatar A, Raphael Karikachery A, Katti KK, Katti KV. Green Nanotechnology of Yucca filamentosa- Phytochemicals- Functionalized Gold Nanoparticles—Antitumor Efficacy Against Prostate and Breast Cancers. *Nanotechnol Sci Appl*. 2023;16:19–40. doi:10.2147/NSA.S437812
5. De Barros CHN, GCF Cruz, W Mayrink, et al. Bio-based synthesis of silver nanoparticles from Orange waste: effects of distinct biomolecule coatings on size, morphology, and antimicrobial activity. *Nanotechnol Sci Appl*. 2018;11:1–14. doi:10.2147/NSA.S156115
6. Ahamed M, Siddiqui MA, Akhtar MJ, et al. Genotoxic potential of copper oxide nanoparticles in human lung epithelial cells. *Biochem Biophys Res Commun*. 2010;396:578–583. doi:10.1016/j.bbrc.2010.04.156
7. Nations S, Long M, Wages M, et al. Subchronic and chronic developmental effects of copper oxide (CuO) nanoparticles on Xenopus laevis. *Chemosphere*. 2015;135:166–174. doi:10.1016/j.chemosphere.2015.03.078
8. Wozniak-Budych MJ, Przysiecka Ł, Maciejewska BM, et al. Facile Synthesis of Sulfobetaine-Stabilized Cu_2O Nanoparticles and Their Biomedical Potential. *ACS Biomater Sci Eng*. 2017;3:3183–3194. doi:10.1021/acsbiomaterials.7b00465
9. Athinarayanan J, Periasamy VS, Krishnamoorthy R, et al. Evaluation of antibacterial and cytotoxic properties of green synthesized Cu_2O/Graphene nanosheets. *Mater Sci Eng C*. 2018;93:242–253. doi:10.1016/j.msec.2018.07.073
10. Ng CHB, Fan WY. Shape Evolution of Cu_2O Nanostructures via Kinetic and Thermodynamic Controlled Growth. *Phys J Chem B*. 2006;110:20801–20807. doi:10.1021/jp061835k
11. Ogwu AA, Darma TH, Bouquerel E. Electrical resistivity of copper oxide thin films prepared by reactive magnetron sputtering. *J Achiev Mater Manuf Eng*. 2007;24:172–177.
12. Elfadill NG, Hashim MR, Chahrour KM, Bououdina M, et al. The influence of Cu2O crystal structure on the Cu_2O/ZnO heterojunction photovoltaic performance. *Superlattices Microstruct*. 2015;85:908–917. doi:10.1016/j.spmi.2015.07.010
13. Ungeheuer K, Marszalek KW, Mitura-Nowak M, et al. Cuprous Oxide Thin Films Implanted with Chromium Ions—Optical and Physical Properties Studies. *Int J Mol Sci*. 2022;23: 8358:1–14. doi:10.3390/ijms23158358
14. Marathey P, Khanna S, Pati R, Mukhopadhyay I, Ray A. Low temperature–controlled synthesis of hierarchical $Cu_2O/Cu(OH)_2$/CuO nanostructures for energy applications. *J Mater Res*. 2019;34:3173–3185. doi:10.1557/jmr.2019.231

15. Ouyang J, Yang H, Tang A. Shape controlled synthesis and optical properties of Cu_2O micro-spheres and octahedrons. *Mater Des*. 2016;92:261–267. doi:10.1016/j.matdes.2015.12.012
16. Maity T, Jain S, Solra M, Barman S, Rana S. Robust and Reusable Laccase Mimetic Copper Oxide Nanozyme for Phenolic Oxidation and Biosensing. *ACS Sustain Chem Eng*. 2022;10:1398–1407. doi:10.1021/acssuschemeng.1c06340
17. Racik KM, Manikandan A, Mahendiran M, Prabakaran P, Madhavan J, Raj MV. Fabrication of manganese oxide decorated copper oxide (MnO_2 /CuO) nanocomposite electrodes for energy storage supercapacitor devices. *Physica E*. 2020;119:114033. doi:10.1016/j.physe.2020.114033
18. Zhang C, Lu L, Hao S, et al. Core-shell Cu2O@CuS@NiCo layered double hydroxide composites as supercapacitor electrode materials. *J Energy Storage*. 2024;77:109983. doi:10.1016/j.est.2023.109983
19. Xue H, Wen X, Fu C, et al. Solar Energy Conversion and Electron Storage by a Cu_2O/CuO Photocapacitive Electrode. *Energies*. 2023;16:3231. doi:10.3390/en16073231
20. Ma C, Wang W, Li W, et al. Full solar spectrum-driven Cu2O/PDINH heterostructure with enhanced photocatalytic antibacterial activity and mechanism insight. *J Hazard Mater*. 2023;448:130851. doi:10.1016/j.jhazmat.2023.130851
21. Guzman M, Arcos M, Dille J, Godet S, Rousse C. Effect of the Concentration of NaBH4 and N2H4 as Reductant Agent on the Synthesis of Copper Oxide Nanoparticles and its Potential Antimicrobial Applications. *Nano Biomed Eng*. 2018;10:392–405.10.5101/nbe.v10i4.p392–405.
22. Chen X, Cui K, Hai Z, et al. Hydrothermal synthesis of Cu2O with morphology evolution and its effect on visible-light photocatalysis. *Mater Lett*. 2021;297:129921. doi:10.1016/j.matlet.2021.129921
23. Suzuki K, Tanaka N, Ando A, Takagi H. Optical Properties and Fabrication of Cuprous Oxide Nanoparticles by Microemulsion Method. *J Am Ceram Soc*. 2011;94:2379–2385. doi:10.1111/j.1551-2916.2011.04413.x
24. Ahmadi H, Khalaj G, Soleymani F, Moalem M, Pourabdollah M, Mahmoudan M. Electrochemical synthesis and characterization of Cu_2 O nanoparticles: effect of electrolyte composition. *J Solid State Electrochem*. 2024;28:2269–2281. doi:10.1007/s10008-023-05757-7
25. Peng Y, Feng Y, Tao Y, Wan H. Preparation of nanoparticles-assembled Cu2O microspheres by ultrasound- assisted polyol process and their adsorption performance. *Desalin Water Treat*. 2022;270:236–244. doi:10.5004/dwt.2022.28746
26. Chen R, Wang Z, Zhou Q, Lu J, Zheng M. A Template-Free Microwave Synthesis of One-Dimensional Cu_2O Nanowires with Desired Photocatalytic Property. *Materials*. 2018;11:1843. doi:10.3390/ma11101843
27. Long J, Dong J, Wang X, et al. Photochemical synthesis of submicron- and nano-scale Cu_2O particles. *J Colloid Interface Sci*. 2009;333:791–799. doi:10.1016/j.jcis.2009.02.036
28. Alahmadi M, Alsaedi WH, Alsulami AH, et al. Synergistic antimicrobial and anticancer effects of WS2/Reduced graphene oxide nanocomposites. *Mater Chem Phys*. 2025;345(1):131299. doi:10.1016/j.matchemphys.2025.131299
29. Pricop A, Negrea A, Pascu B, et al. Copper Nanoparticles Synthesized by Chemical Reduction with Medical Applications. *Int J Mol Sci*. 2025;26(4):1628. doi:10.3390/ijms26041628
30. Fuku X, Modibedi M, Mathe M. Green synthesis of Cu/Cu_2O/CuO nanostructures and the analysis of their electrochemical properties. *SN Appl Sci*. 2020;2:902. doi:10.1007/s42452-020-2704-5
31. Meena J, Kumaraguru N, Shin P, et al. Copper oxide nanoparticles fabricated by green chemistry using Tribulus terrestris seed natural extract-photocatalyst and green electrodes for energy storage device. *Sci Rep*. 2023;13:22499. doi:10.1038/s41598-023-49706-w
32. Kovács D, Radnoczi GZ, Horváth ZE, et al. Photoassisted Chemical Transformation of Cu_2O Nanooctahedra into Cu_2S Quantum-Dot Superstructures: structural and Photoelectrochemical Properties. *ACS Materials Au*. 2025;5:1018–1028. doi:10.1021/acsmaterialsau.5c00106
33. Naz S, Gul A, Zia M, et al. Synthesis, biomedical applications, and toxicity of CuO nanoparticles. *Appl Microbiol Biotechnol*. 2023;107:1039–1061. doi:10.1007/s00253-023-12364-z
34. Togashi T, Hitaka H, Ohara S, et al. Controlled reduction of Cu^{2+} to Cu^{+} with an N,O-type chelate under hydrothermal conditions to produce Cu_2O nanoparticles. *Mater Lett*. 2010;64:1049–1051. doi:10.1016/j.matlet.2010.02.003
35. Yang C, Xiao F, Wang J. 3D flower- and 2D sheet-like CuO nanostructures: microwave-assisted synthesis and application in gas sensors. *Sensors Actuators B Chem*. 2015;207:177–185. doi:10.1016/j.snb.2014.10.063
36. Bhuvaneshwari S, Gopalakrishnan N. Hydrothermally synthesized Copper Oxide (CuO) superstructures for ammonia sensing. *J Colloid Interface Sci*. 2016;480:76–84. doi:10.1016/j.jcis.2016.07.004
37. Filipič G, Cvelbar U. Copper oxide nanowires: a review of growth. *Nanotechnology*. 2012;23:194001. doi:10.1088/0957-4484/23/19/194001
38. Nowak A, Szade J, Talik E, et al. Structural, spectroscopic and biological investigation of copper oxides nanoparticles with various capping agents. *Mater Chem Phys*. 2014;145:465–470. doi:10.1016/j.matchemphys.2014.02.049
39. Zhang F, Zhu A, Luo Y, et al. CuO Nanosheets for Sensitive and Selective Determination of H2S with High Recovery Ability. *J Phys Chem C*. 2010;114:19214–19219. doi:10.1021/jp106098z
40. Chen W, Zhang W, Chen L, Zeng L, Wei M. Facile synthesis of Cu2O nanorod arrays on Cu foam as a self-supporting anode material for lithium ion batteries. *J Alloys Compd*. 2017;723:172–178. doi:10.1016/j.jallcom.2017.06.153
41. Qin Y, Zhang F, Chen Y, et al. Hierarchically Porous CuO Hollow Spheres Fabricated via a One-Pot Template-Free Method for High-Performance Gas Sensors. *J Phys Chem C*. 2012;116:11994–12000. doi:10.1021/jp212029n
42. Mallik M, Monia S, Gupta M, et al. Synthesis and characterization of Cu2O nanoparticles. *J Alloys Compd*. 2020;829:154623. doi:10.1016/j.jallcom.2020.154623
43. Spiridonov VV, Liu XY, Zezin SB, et al. Hybrid nanocomposites of carboxymethyl cellulose cross-linked by in-situ formed Cu2O nanoparticles for photocatalytic applications. *J Organomet Chem*. 2020;914:121180. doi:10.1016/j.jorganchem.2020.121180
44. Liu B, Yao X, Zhang Z, et al. Synthesis of Cu_2O Nanostructures with Tunable Crystal Facets for Electrochemical CO_2 Reduction to Alcohols. *ACS Appl Mater Interfaces*. 2021;13:39165–39177. doi:10.1021/acsami.1c03850
45. Salgado P, Rubilar O, Salazar C, Márquez K, Vidal G. In Situ Synthesis of Cu_2O Nanoparticles Using Eucalyptus globulus Extract to Remove a Dye via Advanced Oxidation. *Nanomaterials*. 2024;14(13):1087. doi:10.3390/nano14131087
46. Aslam M, Schultz EA, Sun T, Meade T, Dravid VP. Synthesis of Amine-Stabilized Aqueous Colloidal Iron Oxide Nanoparticles. *Cryst Growth Des*. 2007;7:471–475. doi:10.1021/cg060656p
47. Bouazizi N, Vieillard J, Samir B, et al. Advances in Amine-Surface Functionalization of Inorganic Adsorbents for Water Treatment and Antimicrobial Activities: a Review. *Polymers*. 2022;14:378. doi:10.3390/polym14030378

48. Negrescu AM, Killian MS, Raghu SNV, et al. Metal Oxide Nanoparticles: review of Synthesis, Characterization and Biological Effects. *Funct J Biomater*. 2022;13:274. doi:10.3390/jfb13040274
49. Kumar M, Ragini Das R, Samal M, et al. Highly stable functionalized cuprous oxide nanoparticles for photocatalytic degradation of methylene blue. *Mater Chem Phys*. 2018;218:272–278. doi:10.1016/j.matchemphys.2018.07.048
50. Aslam M, Schultz EA, Tao S, et al. Synthesis of Amine-stabilized Aqueous Colloidal Iron Oxide Nanoparticles. *Cryst Growth Des*. 2007;7 (3):471–475. doi:10.1021/cg060656p
51. Mott D, Galkowski J, Wang L, et al. Synthesis of Size-Controlled and Shaped Copper Nanoparticles. *Langmuir*. 2007;23:5740–5745. doi:10.1021/la0635092
52. Chakravarty A, Bhowmik K, Mukherjee A, et al. Cu_2O Nanoparticles Anchored on Amine-Functionalized Graphite Nanosheet: a Potential Reusable Catalyst. *Langmuir*. 2015;31(18):5210–5219. doi:10.1021/acs.langmuir.5b00970
53. Khalil KD, Bashal AH, Habeeb T, et al. Cobalt oxide-chitosan based nanocomposites: synthesis, characterization and their potential pharmaceutical applications. *Int J Biol Macromol*. 2023;253(4):126856. doi:10.1016/j.ijbiomac.2023.126856
54. Gapol MAB, Balanay MP, Kim DH. Molecular Engineering of Tetraphenylbenzidine-Based Hole Transport Material for Perovskite Solar Cell. *Phys Chem A*. 2017;121(6):1371–1380. doi:10.1021/acs.jpca.6b12651
55. Swayamprabha SS, Nagar MR, Yadav RAK, et al. Hole-transporting materials for organic light-emitting diodes: an overview. *J Mater Chem C*. 2019;24(7):7144–7158. doi:10.1039/C9TC01712G
56. Bae Y, Li L, Yang K, et al. Fluorination of an N,N,N′,N′-Tetraphenylbenzidine Derivative as a Dopant-Free Hole-Transporting Material for Moisture-Resistant Perovskite Solar Cells. *ACS Appl Energy Mater*. 2021;4(10):10459–10467. doi:10.1021/acsaem.1c01234
57. Saddik MS, Al-Hakkani MF, Abu-Dief AM, et al. Formulation and evaluation of azithromycin-loaded silver nanoparticles for the treatment of infected wounds. *Int J Pharm X*. 2024;7:100245. doi:10.1016/j.ijpx.2024.100245
58. Sreenath K, Suneesh CV, Ratheesh Kumar VK, et al. Cu(II)-Mediated Generation of Triarylamine Radical Cations and Their Dimerization. An Easy Route to Tetraarylbenzidines. *J Org Chem*. 2008;73:3245–3251. doi:10.1021/jo800349n
59. Creason SC, Wheeler J, Nelson RF. Electrochemical and spectroscopic studies of cation radicals. I. Coupling rates of 4-substituted triphenylaminium ion. *J Org Chem*. 1972;37:4440–4446. doi:10.1021/jo00799a034
60. Prabhakaran G, Murugan R. Green synthesis of Cu/Cu_2O/CuO nanostructures and the analysis of their electrochemical properties. *Adv Mater Res*. 2014;938:114–117. doi:10.1007/s42452-020-2704-5
61. Havryliuk O, Rathee G, Blair J, et al. Unveiling the Potential of CuO and Cu_2O Nanoparticles against Novel Copper-Resistant Pseudomonas Strains: an In-Depth Comparison. *Nanomaterials*. 2024;14(20):1644. doi:10.3390/nano14201644
62. Park YD, Lee HB, Yi H, et al. Pseudomonas panacis sp. nov. isolated from the surface of rusty roots of Korean ginseng. *Int J Syst Evol Microbiol*. 2005;55(Pt 4):1721–1724. doi:10.1099/ijs.0.63592-0. PMID: 16014508.
63. Arun KJ, Batra AK, Krishna A, et al. Surfactant Free Hydrothermal Synthesis of Copper Oxide Nanoparticles. *J Am J Mater Sci*. 2015;5 (3A):36–38. doi:10.5923/s.materials.201502.06
64. Hussien A, Ahmed A. Influence of CuO Nanoparticles on the Structural, Optical and Thermal Properties of CMC-PVP Films. *J Nanostruct*. 2025;15(1):239–248. doi:10.22052/JNS.2025.01.023
65. Dehno Khalaji AA, Jarosova M, Machek P. The Preparation, structural characterization, optical properties, and antibacterial activity of the CuO/Cu2O nanocomposites prepared by the facile thermal decomposition of a new copper precursor. *Nanomed J*. 2020;7(3):231–236. doi:10.22038/nmj.2020.07.0007
66. Sharma D, Thakur N, Vashistt J, Bisht GS. Antibacterial Evaluation of Cuprous Oxide Nanoparticles Synthesized Using Leaf Extract of Callistemon viminalis. *Ind J Pharm Educ Res*. 2018;52(3):449–455. doi:10.5530/ijper.52.3.52
67. Zayyoun N, Bahmad L, Laânab LB, Jaber B. The effect of pH on the synthesis of stable Cu2O/CuO nanoparticles by sol–gel method in a glycolic medium. *Appl Phys A*. 2016;122:488. doi:10.1007/s00339-016-0024-9
68. Dodoo-Arhin D, Leoni M, Scardi P, et al. Synthesis, characterisation and stability of Cu_2O nanoparticles produced via reverse micelles microemulsion. *Mater Chem Phys*. 2010;122(2–3):602–608. doi:10.1016/j.matchemphys.2010.03.053
69. Pawar S, Kim J, Inamdar A, et al. Multi-functional reactively-sputtered copper oxide electrodes for supercapacitor and electro-catalyst in direct methanol fuel cell applications. *Sci Rep*. 2016;6:21310. doi:10.1038/srep21310
70. Guzman M, Tian W, Walker C. Obtaining Cu_2O nanoparticles doped with Lanthanum, Magnesium and Manganese using a displacement reaction. In: 2022 IEEE 22nd. Int. Conf. Nanotechnol. 2022. pp. 124–127.
71. Guzman M, Tian W, Walker C, et al. Copper oxide nanoparticles doped with lanthanum, magnesium and manganese: optical and structural characterization. *R Soc Open Sci*. 2022;9:220485. doi:10.1098/rsos.220485
72. Lam NH, Smith RP, Le N, et al. Evaluation of the Structural Deviation of Cu/Cu2O Nanocomposite Using the X-ray Diffraction Analysis Methods. *Crystals*. 2022;12:566. doi:10.3390/cryst12040566
73. Mikrajuddin A, Khairurrijal K. Derivation of Scherrer relation using an approach in basic physics course. *J Nanosci Nanotechnol*. 2008;1 (1):28–32.
74. Azizian-Shermeh O, Einali A, Ghasemi A. Rapid biologically one-step synthesis of stable bioactive silver nanoparticles using Osage Orange (Maclura pomifera) leaf extract and their antimicrobial activities. *Adv Powder Technol*. 2017;28(12):3164–3171. doi:10.1016/j.apt.2017.10.001
75. Li X, Shang Y, Lin J, et al. Temperature-Induced Stacking to Create Cu_2O Concave Sphere for Light Trapping Capable of Ultrasensitive Single-Particle Surface-Enhanced Raman Scattering. *Adv Funct Mater*. 2018;28:1801868. doi:10.1002/adfm.201801868
76. Wang Y, Huang D, Zhu X, et al. Surfactant-free synthesis of Cu_2O hollow spheres and their wavelength-dependent visible photocatalytic activities using LED lamps as cold light sources. *Nanoscale Res Lett*. 2014;9:1–8. doi:10.1186/1556-276X-9-624
77. Filiz BC. The role of catalyst support on activity of copper oxide nanoparticles for reduction of 4-nitrophenol. *Adv Powder Technol*. 2020;31 (9):3845. doi:10.1016/j.apt.2020.07.026
78. Abdulshahed RH, Obeid AK. Assessment of eruca sativa leaves extract ZnO NPs effect on the adverse effects of creatine - induced testes injury. *J Kerbala Agric Sci*. 2024;11:192–208. doi:10.59658/jkas.v11i3.2351
79. Jiang X. Fabrication and nanoroughness characterization of specific nanostructures and nanodevice. Ph.D. thesis, University of Birmingham. 2011.

80. Bhardwaj AK, Kumar V, Pandey V, Naraian R. Bacterial killing efficacy of synthesized rod shaped cuprous oxide nanoparticles using laser ablation technique. *SN Appl Sci*. 2019;1:1426. doi:10.1007/s42452-019-1283-9
81. Swarnkar RK, Singh SC, Gopal R. Effect of aging on copper nanoparticles synthesized by pulsed laser ablation in water: structural and optical characterizations. *Bull Mater Sci*. 2011;34:1363–1369. doi:10.1007/s12034-011-0329-4
82. Ceja-Romero LR, Ortega-Arroyo L, Ortega Rue da De León JM, et al. Green chemistry synthesis of nano-cuprous oxide. *IET Nanobiotechnol*. 2016;10:39–44. doi:10.1049/iet-nbt.2015.0026
83. Dehno Khalaji A, Jarosova M, Machek P. The Preparation, structural characterization, optical properties, and antibacterial activity of the CuO/Cu_2O nanocomposites prepared by the facile thermal decomposition of a new copper precursor. *Nanomed J*. 2020;7(3):231–236. doi:10.22038/NMJ.2020.07.0007
84. Sahai A, Goswami N, Kaushik SD, Tripathi S. $Cu/Cu_2O/CuO$ nanoparticles: novel synthesis by exploding wire technique and extensive characterization. *Appl Surf Sci*. 2016;390:974–983. doi:10.1016/j.apsusc.2016.09.005
85. Ren Y, Ma Z, Bruce PG. Transformation of mesoporous Cu/Cu_2O into porous Cu_2O nanowires in ethanol. *CrystEngComm*. 2012;14:2617–2620. doi:10.1039/C2CE25045D
86. Kumar N, Parui SS, Limbu S, Mahato DK, Tiwari N, Narayan Chauhan R. Structural and optical properties of sol–gel derived CuO and Cu_2 O nanoparticles. *Mater Today Proc*. 2021;41(2):237–241. doi:10.1016/j.matpr.2020.08.800
87. Singh M, Goyal M, Devlal K. Size and shape effects on the band gap of semiconductor compound nanomaterials. *J Taibah Univ Sci*. 2018;12 (4):470. doi:10.1080/16583655.2018.1473946
88. Jun YW, Choi CS, Cheon J. Size and shape controlled ZnTe nanocrystals with quantum confinement effect. *Cheon J Chem Commun*. 2001;1:101. doi:10.1039/B008376N
89. Hassanien AS, Akl AA. Influence of composition on optical and dispersion parameters of thermally evaporated non-crystalline Cd50S50−xSex thin films. *J Alloys Compd*. 2015;648:280. doi:10.1016/j.jallcom.2015.06.231
90. Awan SU, Hasanain SK, Hassnain JG. Defects induced luminescence and tuning of bandgap energy narrowing in ZnO nanoparticles doped with Li ions. *J Appl Phys*. 2014;116:083510. doi:10.1063/1.4894153
91. Chinnaiah K, Maik V, Kannan K, et al. Experimental and Theoretical Studies of Green Synthesized Cu_2O Nanoparticles Using Datura Metel L. *J Fluoresc*. 2022;32:559–568. doi:10.1007/s10895-021-02880-4
92. Mallik M, Monia S, Gupta M, Ghosh A, Prakash Toppo M, Roy H. Synthesis and characterization of Cu_2O nanoparticles. *J Alloys Compd*. 2020;829:154623. doi:10.1016/j.jallcom.2020.154623
93. Sudha V, Murugadoss G, Thangamuthu R. Structural and morphological tuning of Cu-based metal oxide nanoparticles by a facile chemical method and highly electrochemical sensing of sulphite. *Sci Rep*. 2021;11:3413. doi:10.1038/s41598-021-82741-z
94. Kumar N, Sundar Parui S, Limbu S, Kumar Mahato D, Tiwari N, Narayan Chauhan R. Structural and optical properties of sol–gel derived CuO and Cu_2O nanoparticles. *Mater Today Proc*. 2021;41(2):237–241. doi:10.1016/j.matpr.2020.08.800
95. Osorio-Rivera D, Torres-Delgado G, Márquez-Marín J, Castanedo-Pérez JRM, Aguilar-Frutis A, Zelaya-ángel O. Cuprous oxide thin films obtained by spray-pyrolysis technique. *J Mater Sci Mater Electron*. 2018;29:851–857. doi:10.1007/s10854-017-7980-5
96. Akter J, Prasad Sapkota K, Abu Hanif M, Akherul Islam M, Ghulam AH, Ryang HJ. Kinetically controlled selective synthesis of Cu_2O and CuO nanoparticles toward enhanced degradation of methylene blue using ultraviolet and sun light. *Mater Sci Semicond Process*. 2020;123:105570. doi:10.1016/j.mssp.2020.105570
97. Dagher S, Haik Y, Ayesh AI, Tit N. Synthesis and optical properties of colloidal CuO nanoparticles. *J Lumin*. 2014;151:149–154. doi:10.1016/j.jlumin.2014.02.015
98. Sadegh F, Modarresi-Alam AR, Noroozifar M, et al. Solid-state synthesis of PANI-TiO_2 nanocomposite: investigation of reaction conditions, nature of oxidant and electrical properties. *Express Polym Lett*. 2021;15(15):2–15. doi:10.3144/expresspolymlett.2021.2
99. Wu N, Wu H, Zhang J, et al. $Cu_2O/Cu@C$ nanosheets derived from one novel Cu (II) metal-organic framework for high performance supercapacitors. *J Alloys Compd*. 2011;856:157466. doi:10.1016/j.jallcom.2020.157466
100. Aljaafari A, Parveen N, Ahmad F, Waqas Alam M, Ali Ansari S. Self-assembled Cube-like Copper Oxide Derived from a Metal-Organic Framework as a High-Performance Electrochemical Supercapacitive Electrode Material. *Sci Rep*. 2019;9:9140. doi:10.1038/s41598-019-45557-6
101. Kumar R, Rai P, Sharma A. Facile synthesis of Cu2O microstructures and their morphology dependent electrochemical supercapacitor properties. *RSC Adv*. 2016;6:3815–3822. doi:10.1039/C5RA20331G
102. Chatterjee S, Pa AJ. Introducing Cu_2O Thin Films as a Hole-Transport Layer in Efficient Planar Perovskite Solar Cell Structures. *J Phys Chem C*. 2016;120(3):1428–1437. doi:10.1021/acs.jpcc.5b11540
103. Valadbeigi E, Modarresi-Alam AR, Noroozifar M, et al. Synthesis and characterization of new nanocomposites of [poly(o-toluidine)]/(WO3 nanoparticles) and their application in novel hybrid solar cells. *Express Polym Lett*. 2022;16(9):939–959. doi:10.3144/expresspolymlett.2022.69
104. Bhosale MA, Bhanage BM. A simple approach for sonochemical synthesis of Cu_2O nanoparticles with high catalytic properties. *Adv Powder Technol*. 2016;27(1):238–244. doi:10.1016/j.apt.2015.12.008
105. Alsaedi WH, Mohamed WS, Qasem HA, et al. Fabrication of CuO/PdO nanocomposites for biomedical applications. *Inorg Chem Commun*. 2024;170(1):113166. doi:10.1016/j.inoche.2024.113166
106. Asmat-Campos D, Montes de Oca-Vásquez G, Rojas-Jaimes J, et al. Cu_2O nanoparticles synthesized by green and chemical routes, and evaluation of their antibacterial and antifungal effect on functionalized textiles. *Biotechnol Rep*. 2023;37:e00785. doi:10.1016/j.btre.2023.e00785
107. Srivastava P, Kim Y, Cho H. Synergistic Action between Copper Oxide (CuO) Nanoparticles and Anthraquinone-2-Carboxylic Acid (AQ) against *Staphylococcus aureus*. *J Compos Sci*. 2023;7(4):135. doi:10.3390/jcs7040135
108. Msimango LD, Abolarinwa TO, Ojelere O, et al. Structural characterisation of green-synthesised CuO nanoparticles from different precursor sources and their antibacterial activity. *Nano Express*. 2025;6:045006. doi:10.1088/2632-959X/ae15ad
109. Ma X, Zhou S, Xu X, Du Q. Copper-containing nanoparticles: mechanism of antimicrobial effect and application in dentistry-a narrative review. *Front Surg*. 2022;5(9):905892. doi:10.3389/fsurg.2022.905892. PMID: 35990090; PMCID: PMC9388913.
110. Azizian-Shermeh O, Jalali-Nezhad AA, Taherizadeh M, Facile QA. Low-Cost and Rapid Phytosynthesis of Stable and Eco-friendly Silver Nanoparticles Using Boerhavia elegans (Choisy) and Study of Their Antimicrobial Activities. *J Inorg Organomet Polym*. 2021;31:279–291. doi:10.1007/s10904-020-01691-7

111. Verma A, Bharadvaja N. Plant-Mediated Synthesis and Characterization of Silver and Copper Oxide Nanoparticles: antibacterial and Heavy Metal Removal Activity. *J Clust Sci*. 2022;33:1697–1712. doi:10.1007/s10876-021-02091-8
112. Asmat-Campos D, Montes de Oca-Vasquez G, Rojas-Jaimes J, et al. Cu_2O nanoparticles synthesized by green and chemical routes, and evaluation of their antibacterial and antifungal effect on functionalized textiles. *Biotechnol Rep*. 2023;37:e00785. doi:10.1016/j.btre.2023.e00785
113. Lange A, Matuszewski A, Kutwin M, Ostrowska A, Jaworski S. Farnesol and Selected Nanoparticles (Silver, Gold, Copper, and Zinc Oxide) as Effective Agents Against Biofilms Formed by Pathogenic Microorganisms. *Nanotechnol Sci Appl*. 2024;17:107–125. doi:10.2147/NSA.S457124